

Universitat Autònoma de Barcelona
Institut de Ciència de Materials de Barcelona (ICMAB-CSIC)
Nanopto

On Improving the Efficiency of Organic Photovoltaic Devices: Novel Strategies

Martí Gibert Roca

Under the supervision and tutoring of:

Mariano Campoy Quiles

Contents

Chapter 1: Organic Solar Cells and Heat	1
1.1 Introduction	2
1.2 State of the Art	7
1.2.1 Temperature Irreversible Transformations	7
1.2.2 Temperature Reversible Processes	9
1.3 Materials and Methods	10
1.4 Hot n' Cold Setup	13
1.4.1 Concept and Construction	13
1.4.2 Software and Operation	22
1.5 Photoactive Materials Screening	25
1.5.1 Temperature Dependent Electrical Characterization	29
1.5.2 Further Characterization	32
1.5.3 Conclusions	45

Appendices

1.A Voc Calculations	47
1.B PLA Salt Remelting/Annealing	49
1.B.1 Circuit Design	52
1.C Drift Diffusion Simulations Supplementary	57
Bibliography	57

List of Tables

1.1	Reversible and irreversible change coefficients calculated from the ratio between the initial and final efficiencies (Irreversible Change) after one thermal cycling and the efficiency ratio between the initial and the efficiency at the highest temperature (348 K) (Reversible Change).	28
-----	--	----

List of Figures

1.1	Temperature evolution of the efficiency of a commercial OPV device (bottom green) and a commercial silicon PV device (top blue). Device temperature versus time (red line). Figure adapted with explicit permission from the work published in J. Mater. Chem. C, 2021,9, 2123-2132 ¹	5
1.2	Complete device with an active layer thickness gradient resulting in 24 (12+12) different thickness solar cells, on a pre-scale up substrate deposited via blade coating with a decelerating blade speed.	11
1.3	Measuring setup for the preliminary experiments with a hotplate and cells connected using alligator clips. The paper is to insulate the alligator clips from the metallic base.	13
1.4	Exploded view of the complete “Hot n’ cold” Setup, with all the elements tagged and numbered from top to bottom.	16
1.5	View of the basic elements that compose the Hot n’ Cold setup, which are the basis for the entire contraption.	17
1.6	(a) Copper block round stock before machining it (right) and after (left). (b) Hand mill machining during mechanization process.	18

1.7	Semi-exploded view of the top elements that keep the copper block, the thermoelectric modules and the substrate firmly clamped together to ensure good thermal contact. It also keeps the pogo pins in place to ensure good electrical contact.	19
1.8	Old main block (4) version where we can see all the connections exposed and the rib cage (6) holding them separate, as well as holding the pogo pins in place. . .	20
1.9	Bottom view of the “Hot n’ Cold Setup” showing the various control circuit boards as well as the frame and the legs which provide mechanical support to the entire structure.	21
1.10	Image of the thermal control circuit attached to the heatsink through 4 MOS-FETs, with a base below for additional mechanical support	21
1.11	Pictures of the finished “Hot n’ cold” setup both from a top view (a) and a bottom view (b).	23
1.12	QR code to access the repository with all files related to the fabrication of the “Hot n’ Cold” setup.	23
1.13	Graphical user interface front view of the control software that operates the entire “Hot n’ cold” setup, controlling the temperature and the JV measurements simultaneously.	24
1.14	PCE evolution as a function of temperature and temperature cycling for different active layer materials that exhibit (a) permanent PCE decrease, (b) reversible PCE decrease, and (c) reversible PCE increase.	26
1.15	Temperature dependent parameters for a complete temperature cycle, of PB-DBT:ITIC based organic solar cells with different active layer thicknesses. Measured parameters are (a) PCE and (b) Jsc, FF and Voc from top to bottom. . .	30

1.16	Temperature dependent parameters for a complete temperature cycle from figure 1.15, plotted using active layer thickness as the X axis. Measured parameters are (a) PCE and (b) Jsc, FF and Voc from top to bottom.	32
1.17	GISAXS spectrum for pristine and annealed PBDBT:ITIC thin films.	33
1.18	GIWAXS intensity maps for pristine and annealed PBDBT:ITIC thin films (left). Integrated GIWAXS spectra for the same films in two components: in plane ($>45^\circ$); and out of plane ($<45^\circ$)	34
1.19	Device model considered in the paper. (a) Representation of a bulk heterojunction organic solar cell device, representing the different layers of the device stack. (b) Energy level diagram representation of the device. Figure adapted with explicit permission from the work of Azzouzi et al. ²	35
1.20	Drift diffusion simulation results, (a) Voc, (b) FF, (c) Jsc and (d) efficiency, for temperature independent recombination rates and charge mobility ($E_{a,k_{for}} = 0$ and $E_{a\mu} = 0$).	37
1.21	Drift diffusion simulation results, (a) Voc, (b) FF, (c) Jsc and (d) efficiency, for temperature dependent recombination rates and temperature independent charge mobility ($E_{a,k_{for}} = 0.4$ and $E_{a\mu} = 0$).	38
1.22	Drift diffusion simulation results, (a) Voc, (b) FF, (c) Jsc and (d) efficiency, for temperature independent recombination rates and temperature dependent charge mobility ($E_{a,k_{for}} = 0$ and $E_{a\mu} = 0.4$).	39
1.23	Drift diffusion simulation results, (a) Voc, (b) FF, (c) Jsc and (d) efficiency, for temperature dependent recombination rates and charge mobility ($E_{a,k_{for}} = 0.4$ and $E_{a\mu} = 0.4$).	40
1.24	EQE curves for four different active layer thicknesses of PBDBT:ITIC based organic solar cells taken at different temperatures ranging from 298 K to 348 K.	43

1.25	SCLC fit results with electron and hole mobilities for PBDBT:ITIC based electron and hole only devices with an active layer thickness of 160 nm side by side with the efficiency of a similar thickness device (163 nm).	44
1.26	3D render of the rib cage (6) without and with sprues added to prevent holes from forming during salt remelting (left). Cross section view of three cylindrical solid samples after salt remelting, showing a bubble formed during the salt remelting process, where all the air pockets entrapped during 3D printing have merged into one big bubble (right).	51
1.27	3D printed piece after being remelted in rough grain salt. The surface of the piece becomes extremely rough and the dimensionality of the piece gets compromised due to the molten PLA flowing outwards into the intergranular space.	51
1.28	(a) H bridge conceptual schematics using 4 switches and one load. (b) Current flow during normal operation. (c) Current flow on short circuit condition.	53
1.29	(a) H bridge conceptual schematics with current direction control circuit based on logic gates. (b) Current direction control circuit operating switches through the logic gates.	54
1.30	(a) H bridge conceptual schematics with current direction control circuit as well as PWM current control circuit. (b) Load current direction and PWM control operating simultaneously.	56
1.31	Manual circuit operation in cooling mode where the green LED indicates that the board receives power, and the blue LED indicates that it is currently cooling the sample.	58
1.32	Schematics of the “Hot n’ cold” PWM H bridge temperature control circuit, showing the different sub-circuits and a brief explanation of their function.	59

1.33 Comparison table for all drift diffusion simulation results explained in section	
1.5.2, including from top to bottom: Voc; FF; Jsc; and efficiency.	60

Chapter 1

Organic Solar Cells and Heat

Abstract

In this chapter we will study the relationship between the performance of high efficiency organic solar cells and temperature. The main hypothesis of this chapter is that the temperature dependence of charge mobility can be exploited to increase OPV performance. In other words, we want to test if the performance of OSC can be increased by mildly heating the active layer. To do so, we will characterize a series of solar cells, based on 10 high efficiency photoactive layer blends, while exposing them to realistic operational temperatures (from 298 K to 348 K), to evaluate the relationship between their electrical performance and active layer temperature.

? Define ?
We have manufactured a series of solar cells, mainly focusing on state of the art materials, such as NFAs, in order to enhance their electrical performance by subjecting them to different temperatures, while trying to avoid irreversible morphological transformations. Our main efforts have been focused on systems based on PBDBT:ITIC active layers, which show significant and highly reversible PCE improvement at higher than ambient temperatures. In the same experiments, we have studied how this temperature-driven performance enhancement depends on the thickness of a given device, as this can be of great technological interest, especially for roll-to-

is this word needed?

roll manufacturing processes. Besides, we have been collaborating with several colleagues, who have performed a series of simulations and morphological characterizations, to better understand the changes this photoactive material undergoes when exposed to different temperature conditions.

As an important part of this chapter, we have designed and built from scratch a fully customized, temperature controllable, substrate holder that can heat up and cool down the solar cells from 273 K to 363 K (0-90°). This setup allowed us to perform a thorough characterization of all the different photoactive material based solar cells, accurately, quickly, easily and in a very repeatable manner within this wide temperature range.

1.1 Introduction

On most solar cells, a significant portion of the incoming sunlight spectrum is not absorbed in the photoactive layer, most of which is either converted into phonons or reflected back into the vastness of space.³⁻⁵ This fraction, which does not have a significant contribution in most conventional PV technologies, mainly consists of NIR and IR photons.⁶⁻⁸ These, otherwise lost photons could be efficiently converted into electrical energy by using a tandem configuration,^{9,10} or even better, a hybrid thermoelectric system that could absorb the energy of the entire IR range.¹¹⁻¹³ However, since these systems are usually cumbersome and expensive, the added complexity and cost ends up not compensating the extra efficiency obtained, especially during the scale up process.^{14,15} A revolutionary alternative would be to directly absorb these photons within a conventional solar cell, using their energy to raise the active layer temperature in order to increase the solar cell's performance.

It is a well known fact that solar cell performance is greatly dependent on temperature.^{16,17}

you could use
i.e., or even
e.g.)

This dependence is generally negative for most solar cell technologies, like bulk silicon and In-GaAs based solar cells, leading to reduced performances at higher temperatures.^{18,19} As we will see in following sections, these reduced efficiencies generally result from a minuscule increase in J_{sc} at higher temperatures, associated to lower bandgaps that lead to the absorption of a slightly wider portion of the spectrum, combined with a significant drop in the V_{oc} of the solar cell, which arises from higher reverse saturation currents²⁰

Even though this trend, where V_{oc} decreases with temperature, is shared amongst the majority of PV technologies, the temperature dependence of other factors, such as absorption, charge mobility and charge recombination will ultimately determine the overall PCE temperature dependence of a solar cell.²¹ In conventional solar cell technologies, these factors do not have a strong dependence with temperature, so they cannot compensate for the significant reduction in both V_{oc} and FF.^{22,23} Nevertheless, in emerging technologies such as OPV, charge mobility is much more dependent on temperature and, whilst the temperature dependence of the V_{oc} is still negative, its variation range is much smaller.²⁴⁻²⁶ This combination makes possible that, for some systems and within certain temperature ranges, organic solar cell performance can increase at higher temperatures.^{27,28} For these systems, higher temperatures have a significant impact in active layer charge mobility, which can heavily affect the FF and the J_{sc} by enhancing charge extraction. This effect is specially pronounced in thicker organic solar cells, which suffer from lower overall electrical conductivity and hindered charge extraction.^{29,30} Within the temperature range where this enhancement in charge mobility overshadows the inevitable decrease in V_{oc} , organic solar cell performance will have a positive relation with temperature.

This phenomenon has been already reported in the literature for widely studied materials such as the ubiquitous P3HT:PC61BM with good results, as we will see in the following sections.^{27,28} The main disadvantage of these systems is that they have been reported to be unstable at elevated temperatures, forming PCBM dimers and undergoing morphological transformations.³¹

Nonetheless, with new higher efficiency blends emerging ever more frequently, the OPV material paradigm is constantly evolving. This paradigm has seen a major change with the advent of NFAs and high efficiency polymers, which provided new active layer compositions, whose temperature dependent performance, to our knowledge, is yet to be thoroughly studied.

As a preliminary proof of concept, Dr. Jurado performed a series of PCE measurements for two commercial solar cell modules, one organic and one based on silicon, while simultaneously measuring their temperature as sunlight was heating them up. These first results, which can be seen in figure 1.1, show two very different behaviours, where the silicon solar cell efficiency quickly drops as it heats up, while the organic one rises. This is a really interesting result, because it clearly shows that the temperature response of organic solar cells is not necessarily the same as that of conventional PV technologies, suggesting the possibility of overall higher performances at higher temperatures. Further details about these experiments can be found in the work published in *J. Mater. Chem. C*, 2021,9, 2123-2132¹

Motivated by the literature and these preliminary results, in collaboration with Dr. Jurado and Dr. Vega as part of a bigger study, we studied the temperature dependent performance of 10 different donor-acceptor blends. These were manufactured with an active layer thickness gradient, which allowed us to assess the effect of temperature in PCE as a function of solar cell thickness. As a result of this material screening study, we decided to perform further electrical and morphological characterization on devices manufactured with PBDBT:ITIC as the active layer, because they exhibited the greatest temperature dependent PCE increase as well as high temperature stability.

In order to perform temperature dependent measurements for all these systems, we needed a way to accurately tune and control the temperature of the samples during the measurements. However, since we use pre-scaling, microscope slide sized substrates, which are not widely used in the world of OPV, there wasn't any commercial solution available for temperature stud-

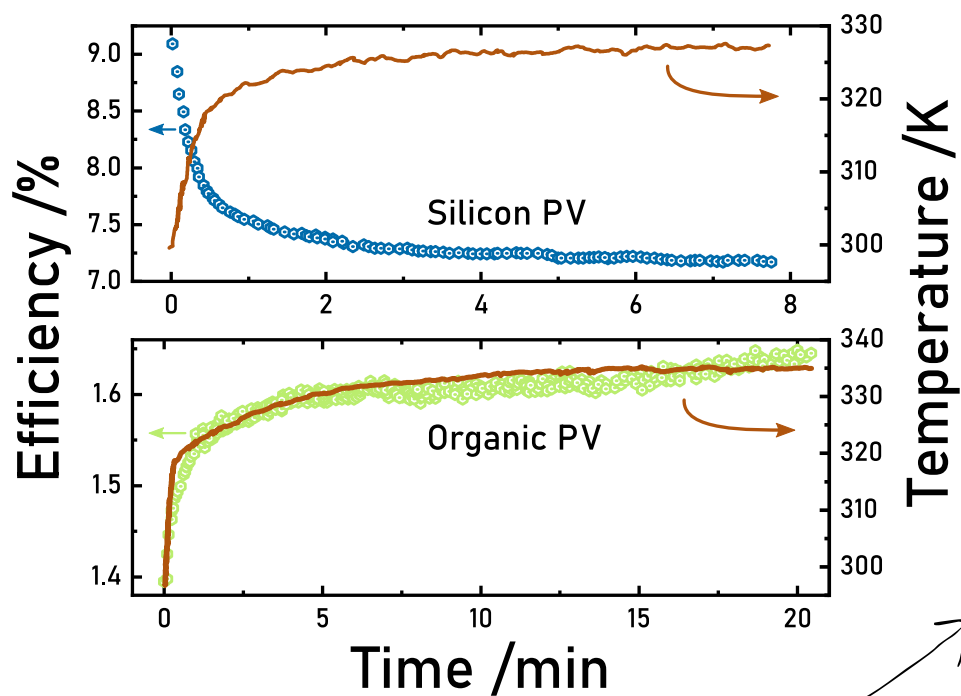


Figure 1.1: Temperature evolution of the efficiency of a commercial OPV device (bottom green) and a commercial silicon PV device (top blue). Device temperature versus time (red line). Figure adapted with explicit permission from the work published in J. Mater. Chem. C, 2021,9, 2123-2132¹

which one?
why "saturation"?
?

ies that conformed with our substrates.³²⁻³⁴ To solve that problem, we decided to build our own temperature regulable holder, by using Peltier elements, which allow us to quickly heat up and cool down our samples anywhere from 273 K all the way up to 363 K (0-90°C). The ability to quickly change the temperature proved to be useful to discern between irreversible and reversible performance changes, where time is a crucial factor. In the same note, we also needed to measure all 24 cells of each substrate as fast as possible at each given temperature, in order to measure them under the same conditions, trying to minimize time related morphological changes. With that in mind, this setup was integrated with the “Pika Demultiplexer”, discussed in previous chapters, to seamlessly switch through every cell as fast as possible, while measuring them all. As part of this chapter, we will explain the entire prototyping process and working principles of this setup.

To further characterize morphological changes, Dr. Edgar Gutiérrez Fernández and Dr. Jaime Martín have analyzed our PBDBT:ITIC active layers before and after thermal cycling using GIWAXS and GISAXS, in order to detect any changes in active layer blend morphology. Paralelly, Dr. Jenny Nelson and Dr. Mohammed Azzouzi performed drift diffusion model simulations, simulating the electrical behaviour of our PBDBT:ITIC based organic solar cells, in order to rationalize the origin of the performance enhancement observed in our experimental results. Besides, as part of his thesis, Dr. Jurado further continued into this study by performing more in depth electrical characterization, performing temperature dependent EQE and mobility measurements, which will be briefly mentioned in this chapter.

My specific role within this project ~~has been focused on~~ the design and manufacture the temperature regulable holder. I have also participated in the fabrication of almost all solar cells used during the study, with a minor contribution on the measurements. Finally, I have collaborated in the data analysis and have extracted my own conclusions from the experiments which are stated ~~in~~ the end of this chapter.

1.2 State of the Art

1.2.1 Temperature Irreversible Transformations

Temperature variations can have non-reversible effects on OSC, which mainly revolve around morphological changes such as phase segregation and recrystallization.^{35,36} These morphology changes are the basis of annealing processes where crucial properties such as charge transport, absorption, or recombination mechanisms, are finely adjusted by tuning film microstructure with different annealing conditions.^{37,38} Selective recrystallization of such films can lead to bigger crystalline domains for both donor and acceptor. Optimum crystalline domain size is usually translated into higher absorption and/or better charge transport properties.^{27,39} Such morphological changes can also affect recombination mechanism ratios, which can be adjusted to lower overall charge recombination by tuning annealing process parameters.⁴⁰

However useful this temperature dependence can be, such irreversible processes play an important role in solar cell degradation, and OSCs are no exception to that rule.^{41–45} Being constantly exposed to the sun, solar cells can experience elevated temperatures (323–353 K). Unfortunately, in many systems, those high temperatures lead to a performance decrease over time.^{46–49} Nonetheless, the temperatures reached during normal OSC operation are far below the decomposition temperature of its composing materials, which means that this thermal instability is more related to structural changes.^{50–52}

Within the active layer, alongside many environmental factors (heat, oxygen, light, and humidity), one of the main degradation processes are the same morphological changes that can otherwise be used to tune the performance of our solar cell.^{53–55} In a way, the active layer is under constant annealing conditions, when exposed to repeated heat cycles caused by temperature shifts between day and night. If we combine this constant temperature cycling with the

fact that the optimal active layer morphology is usually metastable, these constant temperature shifts can accelerate its transition towards a thermodynamic equilibrium, even with moderate temperature variations.^{56–58} This problem can be further exacerbated by the fact that polymer mobility sharply rises above its T_g , potentially leading to immediate device degradation above a certain threshold.^{59–61} This shift towards a thermodynamically stable state is usually associated with significant phase separation, which greatly reduces donor–acceptor interface surface area, thus hindering exciton separation and overall charge transport within the active layer.^{62–64}

Apart from affecting the donor-acceptor interface, temperature can also have a significant effect on the interface between the charge transport layer and its adjacent layers, namely the active layer and the charge collection layer. In the charge transport layer-active layer interface, morphology changes in the latter can create gaps between the two layers, which has been reported to lower the charge extraction efficiency.^{65,66} On the other hand, temperature can dramatically increase the diffusion rate of metal atoms from the contact into the charge transport layers, severely decreasing their selectivity, and lowering overall device performance.^{67–70}

To mitigate these temperature related instabilities, organic solar cell synthetic chemists have turned their attention to the chemical tunability of non-fullerene acceptors. Their synthetic flexibility opens up a new door for blend morphology engineering, offering the possibility to add thermal stability as one of the main priorities. By tuning film deposition conditions and molecular design, they can control the molecular organization behaviour of NFAs within the active layer, greatly decreasing temperature induced morphological changes.⁷¹ There are some examples of such temperature stable NFA based active layer blends in the literature, like PTB7-Th:COi8DFIC, that exhibit optimal donor acceptor miscibility and domain size, endowing the cell with both better performance and improved shelf-life stability.^{72,73} Besides these special cases, general use NFAs have also been reported to undergo reduced performance degradation at higher temperatures, when compared to fullerene-based acceptors, thanks to their higher

reference save review here?

maybe

morphological stability, which arises from a lower molecular diffusion within the active layer, preventing them from aggregating and recrystallizing.⁷⁴ Recent studies show that aggregation and recrystallization are the main driving factors of thermal instability in NFA-based OSC, and they can be mitigated by vitrifying the active layer blend, making it thermally stable.⁷⁵

1.2.2 Temperature Reversible Processes

Besides non-reversible transformations, there are other reversible changes that occur in solar cells when exposed to different temperatures. However, predicting the effect of these changes reliably is not easy, because some characteristics such as charge mobility, exciton generation or recombination, which ultimately determine PCE, are strongly dependent on other parameters such as active layer morphology, thickness and light intensity.⁷⁶⁻⁸⁰ However, within a certain temperature range, active layer blends with a temperature invariant morphology, can exhibit enhanced donor-acceptor electron transfer rates and increased charge mobilities when exposed to higher temperatures, since their main charge transport mechanism is accurately described by thermally activated hopping.^{81,82}

Higher charge mobilities and exciton dissociation rates will be translated into higher J_{sc} with increasing temperatures, which will level off above temperatures where charge mobility is no longer the limiting factor. This is only true within the temperature range where the AL morphology is thermally stable, since, whenever we surpass a certain threshold, morphological changes will distort and overshadow this, otherwise reversible, enhancement.^{27,83}

Higher temperatures can also lead to an increase in the recombination rate, which in combination with charge transport will greatly affect the FF of OPV devices.⁷⁶ These two factors will be in a tight compromise, but as long as charge extraction is not overshadowed by charge recombination, the FF will increase with temperature. As an example, Bagienski et al. found

to prove...
this is hard
Rephrase?

that, for a P3HT:PC61BM solar cell, the fill factor had a positive relation with temperature from 263 K to 343 K, above which the trend reverted towards lower fill factors.^{28,81}

While the temperature dependencies for J_{sc} or FF are slightly more intricate, being indirectly related through charge mobility and recombination, the general relation between V_{oc} and temperature, even though counter-intuitive at first, can be directly derived from the diode equation of the solar cell. As we have already seen in section ?? at first sight the V_{oc} seems to have a positive dependence with temperature (equation 1.1).

$$V_{oc} = \frac{nk_bT}{q} \ln \left(\frac{J_l}{J_0} + 1 \right) \quad (1.1)$$

This is a misleading interpretation of the equation, endorsed by the fact that both experimental data and previously reported literature show the opposite trend. This contradiction arises from the fact that the J_0 term in equation 1.1 is also dependent on temperature, changing much more rapidly than the linear T term. However, this negative trend is less pronounced in organic semiconductors than in their inorganic counterparts, resulting in lower V_{oc} losses at higher temperatures as we will see in future sections. A more in depth exploration on the V_{oc} -temperature relation calculations can be found in the appendix of this chapter.

(remember to link here to an appendix n°1)

1.3 Materials and Methods

In this study, a variety of organic solar cells based on different active layer materials were manufactured and characterized in order to evaluate their temperature dependent performance. These systems were fabricated in collaboration with Dr. Jurado and Dr. Vega as part of a bigger project, in order to identify if there is a general relationship between the performance of

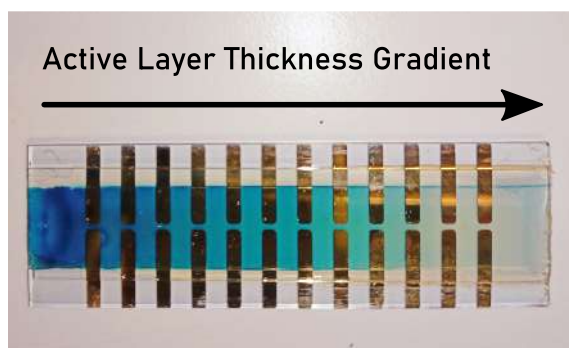


Figure 1.2: Complete device with an active layer thickness gradient resulting in 24 (12+12) different thickness solar cells, on a pre-scale up substrate deposited via blade coating with a decelerating blade speed.

NFA based blends and temperature. Even though we will discuss the results obtained with all studied materials, in this thesis we will mainly focus on results obtained with PBDBT:ITIC active layers, because of its high thermal stability and overall good temperature related performance enhancement.⁸⁴

Devices were fabricated with an inverted architecture, similarly to those of previous chapters, consisting on an ITO substrate, a ZnO nanoparticle based ETL, the photoactive layer, a MoO₃ HTL and the final silver electrode. For a more detailed fabrication procedure description, the reader is referred to chapter ?? In order to study the thickness dependence, the active layers were manufactured with a thickness gradient, by varying the blade coater speed from 80 mm s⁻¹ down to 5 mm s⁻¹, resulting in active layer thicknesses in the range between 300 nm all the way down to 75 nm (figure 1.2). With this deposition configuration, we obtained two cells for each thickness, increasing the reproducibility of our results.

In these measurements each substrate, which consists of 24 pixels, was measured through at least a full heat cycle, which consists in heating the substrate from 293 K to 353 K and then cooling it back down to 293 K. Measuring during substrate heating as well as during cooling provided insight into the reversibility of temperature dependent changes. The temperature

range was chosen to simulate various realistic solar cell operation conditions, from milder, more temperate climates, like southern Europe, to hotter, more extreme climates such as those found in the Arabian peninsula.^{85,86} This temperature range can also simulate the implementation of light absorption-based systems to artificially raise cell temperature by solar photothermal conversion. Besides, these temperature ranges are similar to those used in OPV stability testing.⁸⁷ This temperature dependent performance measurements consisted on individual JV curves for each pixel, performed at 11 temperatures, evenly distributed within the previously mentioned temperature range, resulting in ~ 800 individual JV curves for each material.

In order to study temperature-induced morphological changes, PBDBT:ITIC active layers were deposited using the same conditions onto glass and silicon pristine substrates. These samples were sent to our collaborators Dr. Edgar Gutiérrez Fernández and Dr. Jaime Martín, who characterized their morphology using GIWAXS on the NCD-SWEET beamline at the ALBA synchrotron, and GISAXS on the SAXS beamline at the Elettra synchrotron radiation facility, in Trieste.

Parallely, in collaboration with Dr. Jenny Nelson's group at London Imperial College, Dr. Mohammed Azzouzi performed drift diffusion simulations to investigate how device performance is related to pixel thickness, light intensity and temperature.

As part of his thesis, Dr. Jurado further continued this study by performing temperature dependent EQE measurements, as well as SCLC and light intensity dependent measurements to determine electron and hole mobility at different temperatures.

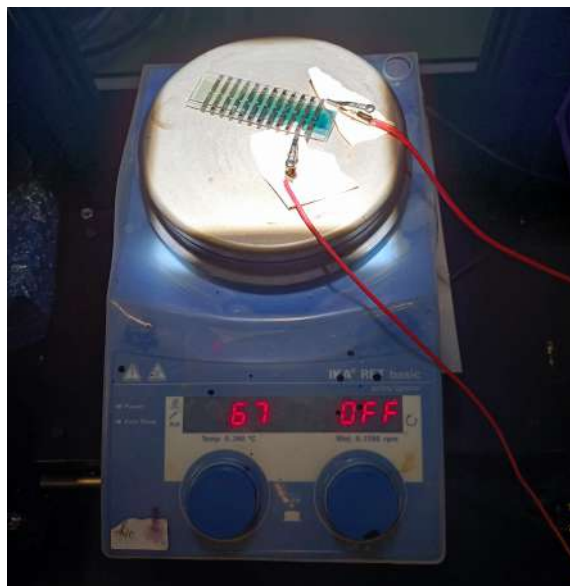


Figure 1.3: Measuring setup for the preliminary experiments with a hotplate and cells connected using alligator clips. The paper is to insulate the alligator clips from the metallic base.

1.4 Hot n' Cold Setup

1.4.1 Concept and Construction

In order to measure our devices at various temperatures, we performed some preliminary experiments by heating them up with a hotplate, while connecting each substrate separately with alligator clips (figure 1.3). As expected, this measurement setup had multiple disadvantages: it did not provide controllable homogeneous temperatures across the substrate; lowering the temperature during the cooling cycle was really slow due to the high thermal mass of the hotplate; and the electrical connections to each of the cells were suboptimal and manually operated. To improve the reproducibility of our results, we tried to acquire a commercial solution for temperature dependent OPV characterization. However, we could not find any commercial solution to perform this study, because of our bigger than usual pre-scale up substrates, which, being more focused on blade coating, are not that commonly used in OPV research. That is why, out of necessity, we decided to build our own setup, which we appropriately named “Hot n’ cold”.

As the first step of the prototyping process, we summarized requisites of the setup, which are the following:

- **Pre-Scale Up Substrate Adaptability:** It has to adapt to our pre-scale up microscope slide-sized substrates, providing electrical contact to each pixel and the ground electrode.
- **Temperature Controllable:** It has to be able to accurately regulate solar cell temperature, which has to be homogeneous along the substrate, and maintain it within a small tolerance.
- **High Athermation*:** It has to be able to heat up and cool down (athermate) quickly, to enable for faster measurements and to prevent non reversible changes from occurring if not desired.
- **Fast Demultiplexing:** It needs to be able to electrically connect the characterization equipment with each of the pixels within a substrate and switch between them as fast as possible, to measure every cell under virtually the same conditions.
- **Small Form Factor:** It needs to be compact enough to be put under the solar simulator and inside the EQE setup, as well as somewhat portable so that it can easily be moved around through these setups.

Taking into account these requirements, the “Hot n’ cold” setup was divided in 3 main components: A modified version of the “**Pika demultiplexer**”, for the electrical connections and demultiplexing; a **temperature management system**, to athermate the substrate as quickly and efficiently as possible; and **custom substrate holder** to affix the substrate to the setup, while electrically connecting each cell to the multiplexer and efficiently transferring heat to and from the substrate.

***Athermate:** Undergo a change in temperature.

- “Internal combustion engines need to be resistant to athermation”

Etymology: Adapted from accelerate (ad-celerare), to change velocity, resulting in athermate (ad-thermare), to change temperature.

→ Reframe title?

Since the temperature management system had to be compact, portable and high power density, the most logical choice was to use Thermoelectric Modules (aka Peltier Modules), which are electrically driven heat pumps based on the thermoelectric effect. Being heat pumps, these modules provide both heating and cooling capabilities integrated in one single device, replacing the need for messy and bulky water cooling systems or slow air cooling solutions, which would have been needed to complement typical electrical resistive heating elements. We are aware that phase change based heat pumps are much more efficient cooling solutions, but at such small scales they really compromised the small form factor of the apparatus without providing any significant advantage over thermoelectric modules.

Over the next paragraphs we will discuss in detail the configuration of the “Hot n’ cold” setup, which can be seen in an exploded vision in figure 1.4. In this chapter we will only discuss the final optimized version of the setup, but we want to note that there have been previous more rudimentary versions that correctly directed us towards the final optimized setup.

Thermoelectric modules do not have the capacity of generating or sinking heat on their own, their working principle is similar to that of a heat pump, where they transfer heat energy from one side of the module to the other when electrically powered. Conveniently, they can be operated in two different modes, being able to pump heat towards either side depending on the current direction flowing through the module. Because of this working principle, in order to reach and maintain high or low temperatures on one side, we needed to place the thermoelectric modules in direct contact with a big enough heatsink that provides a large heat reservoir to source and sink heat from, otherwise the entire module heats up due to resistive losses. That is why, as we can see both in figure 1.4 and in figure 1.5 in more detail, the two thermoelectric elements (8) that power this entire setup are sandwiched between a copper piece (7), which will be in contact with the solar cell substrate (3), and a big heatsink (9), which will act as the constant temperature heat reservoir. To keep a small form factor, we decided to place that heatsink (9) directly below the thermoelectric elements (8), with the copper block on top (7)

Now I get it!

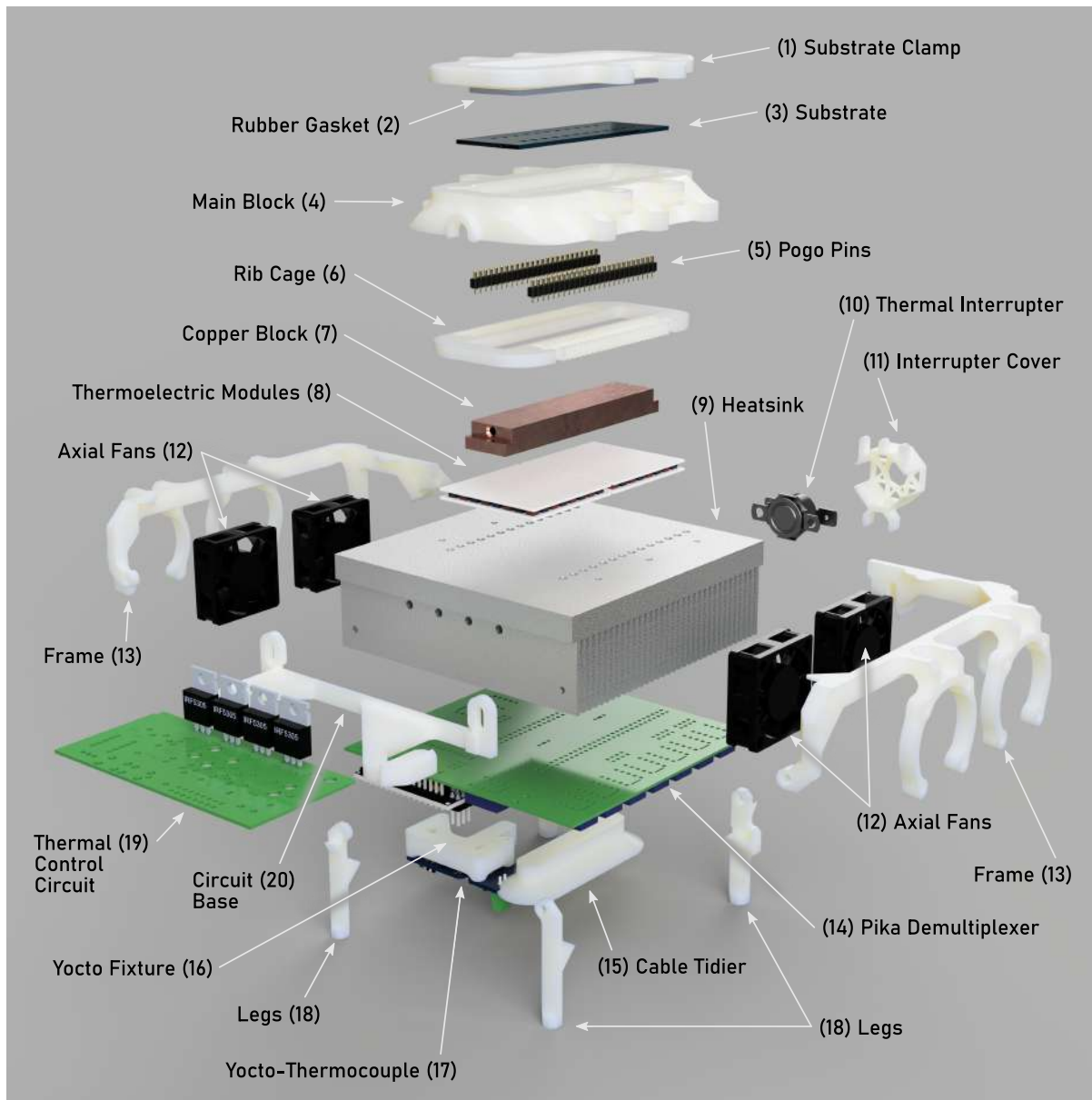


Figure 1.4: Exploded view of the complete “Hot n’ cold” Setup, with all the elements tagged and numbered from top to bottom.

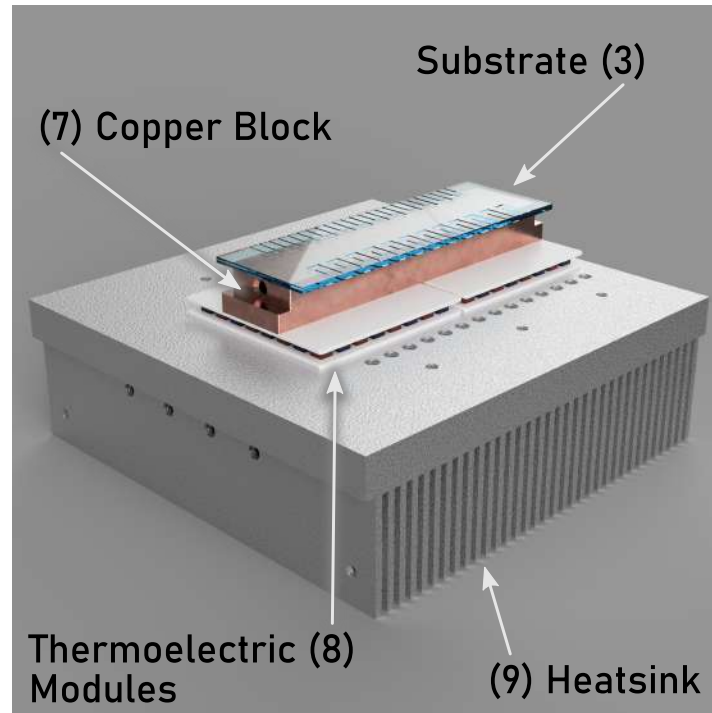


Figure 1.5: View of the basic elements that compose the Hot n' Cold setup, which are the basis for the entire contraption.

(figure 1.5). The choice of placing the heatsink upside down poses a great compromise to its dissipation efficiency, but this was a necessary compromise to keep a compact form factor and enable top cell illumination, so we decided to mitigate the effects later in the design process.

The copper block (7) is used as a heat interface that thermally connects the thermoelectric elements (8), placed below, with the center of the substrate (3), on top (figure 1.5). This copper piece (7) serves both as a buffer, to even out any possible temperature gradients caused by inhomogeneities within the thermoelectrics (8), and as a thermal mass, to smooth any short term temperature fluctuations.

This copper block (7) was carefully machined to be slightly narrower than the substrate, so that the cell terminals on the substrate edge could be electrically contacted without clearance problems, while being able to efficiently transfer heat to the centre of the substrate. The block

→ Challenge?

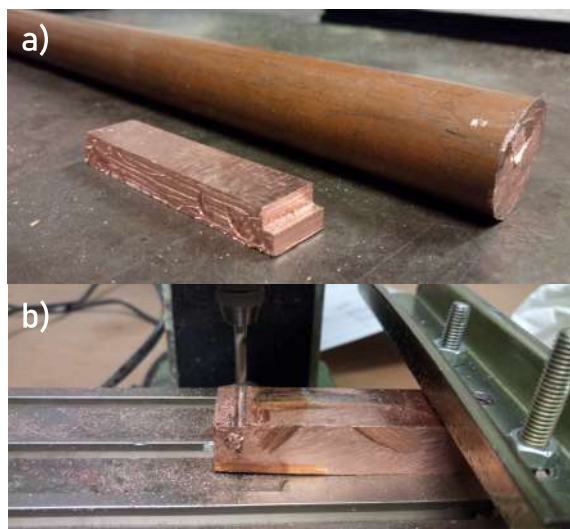


Figure 1.6: (a) Copper block round stock before machining it (right) and after (left). (b) Hand mill machining during mechanization process.

is shaped so that it has two lateral steps that are used to clamp it down to the thermoelectric modules to provide a good thermal interface (figure 1.6). Atop these steps, two lateral holes were drilled to insert two thermocouples that are used to probe the temperature on each side of the block, providing feedback not only on the block's temperature but the temperature distribution, useful to detect a complete failure in one of the thermoelectric modules.

For practical reasons, we decided to keep the multiplexing board (14) outside of this contraption by placing it on the bottom of the heatsink (9). However, since the substrate (3) and the multiplexing board (14) need to be electrically connected, we had to drill several holes through the heatsink (9) to run the contact cables. These cables connect the pogo pins (5) with the bottom multiplexer board (14) (figure 1.8), working as an extension that enables the separation between the substrate and the board, so that we can keep everything as compact and sturdy as possible.

On the top part, in order to hold the substrate (3) onto the copper bar (7), as we can see in figure 1.7, we designed a 3D printed contraption made of **3 separate parts**, which

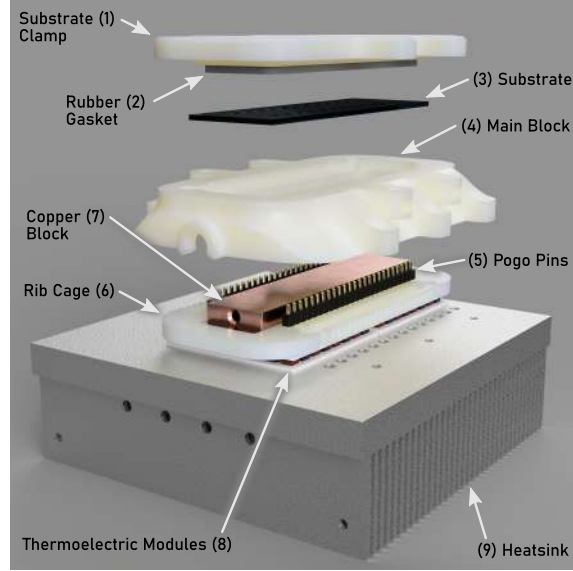


Figure 1.7: Semi-exploded view of the top elements that keep the copper block, the thermoelectric modules and the substrate firmly clamped together to ensure good thermal contact. It also keeps the pogo pins in place to ensure good electrical contact.

are the following: the **rib cage** (6), which holds the cables coming from the bottom of the heatsink (9) and their connections separate (figure 1.8) and wraps around the copper block (7); the **main block** (4), which goes over the rib cage (6) to hold the pogo pins (5) in place and clamps tightly against the heatsink (9), sandwiching together the thermoelectric modules (8) between the copper block (7) and the heatsink (9), and ensuring constant thermal contact, as well as encasing the rib cage (6) with all the connections secured in place; And finally, on top of all that, a separate **substrate clamp** (1), that screws onto the main block (4) to provide pressure between the substrate (3) and the pogo pins (5) to ensure good electrical contact, with a rubber gasket (2) to prevent substrate damage.

In order for the 3D printed parts to hold their shape at the elevated operating temperatures for long periods of time, we performed a remelting/annealing process that endowed the 3D printed parts, which needed to operate at high temperatures with the necessary thermal stability. This process is explained in full detail in this chapter's appendix section 1.B.

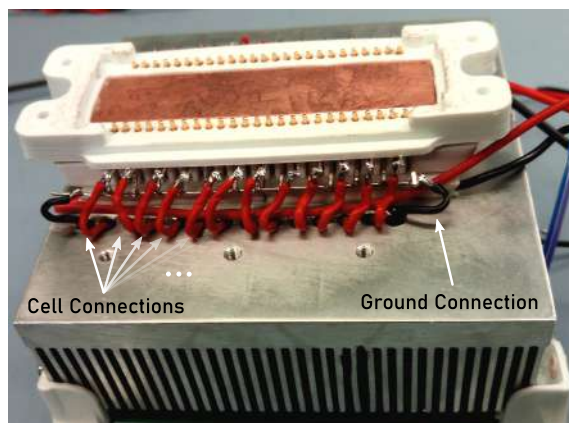


Figure 1.8: Old main block (4) version where we can see all the connections exposed and the rib cage (6) holding them separate, as well as holding the pogo pins in place.

The Pika multiplexing board had to be slightly modified to accommodate two more connections coming out from the Arduino nano into the temperature control circuit. In order to measure the temperature, instead of using the same Arduino, which at this point had all its pins already in use, we implemented a commercial solution: Yoctopuce’s Yocto-Thermocouple (17). This is a USB enabled microcontroller that reads the temperature from the two thermocouples and, by communicating with the Arduino, they can both accurately control the temperature of the substrate. We want to note that, with the latest Pika demultiplexer board, this Arduino pin limitation is completely overcome. That is why, next versions of the “Hot n’ cold” setup, will use the Arduino to read substrate temperature as well as to control the thermoelectrics, making the setup more self-contained.

The Yocto-Thermocouple (17) was attached below the Pika board (14) with a 3D printed fixture (16) directly soldered onto the board, as well as a cable tidier (15) to wind the excess thermocouple cable. In order to hold the multiplexer board (14) in place, and to provide the entire setup with a base for better stability, we added legs (18) and a frame (13), neatly wrapping everything together (figure 1.9). These legs (18) were bolted to the heatsink (9) through threaded holes, and were held on the top by the frame (13) that conformed to the shape of the heatsink (9), wrapping around its corners. This frame (13) has four mounting spots for four

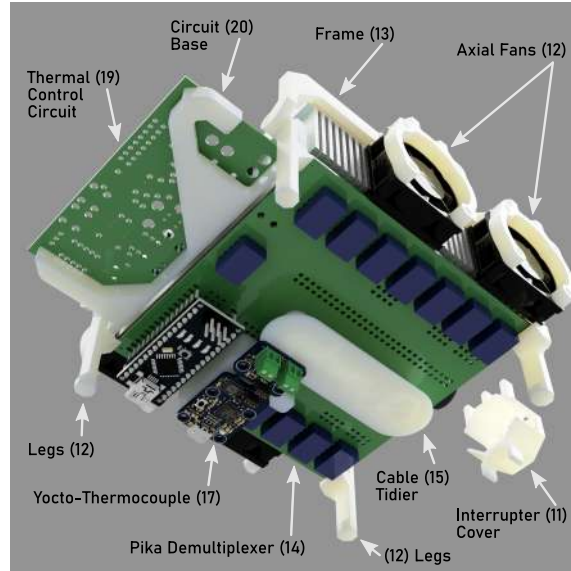


Figure 1.9: Bottom view of the “Hot n’ Cold Setup” showing the various control circuit boards as well as the frame and the legs which provide mechanical support to the entire structure.



Figure 1.10: Image of the thermal control circuit attached to the heatsink through 4 MOSFETs, with a base below for additional mechanical support

axial fans (12) that provide the heatsink (9) with active air cooling, ensuring that it operates efficiently even when placed upside down.

The thermal control circuit (19), further described in section 1.B.1, also has some components that require active cooling, so they are directly attached to the heatsink (9) to dissipate the generated heat, and as a side benefit, they provide an attachment point for the electrical circuit (figure 1.10). To provide extra mechanical support, there is an additional plastic structure (20) below the circuit that prevents the attached electrical components from carrying all the mechanical load during operation.

As a power source we used a DC fixed voltage, 15 V power source that provided up to 22 A, totalling in a max power output of 330 W. This power source also has inrush and overcurrent protection to minimize fire hazards that arise from working with components with power densities on the same order of magnitude of a regular hotplate.⁸⁸

On the same note, we decided to add another layer of fire protection in the form of a fail-safe thermal interrupter (10), chastised by a previously molten setup. This thermal interrupter (10) is directly clamped on the heatsink (9) and completely shuts off the power to the thermoelectric modules (8) if the heatsink (9) is above 60°C. During the failure, the fans (12) are left on, in order to quickly cool down the heatsink (9) so that the experiment can continue, while a bright red LED in the temperature control circuit board (19) indicates that there has been some kind of failure.

The complete fully assembled “Hot n’ cold” setup can be seen in figure 1.11, where both a top and a bottom view show the outside appearance of this contraption. On the top version we can see how the main block perfectly aligns the cell contacts with the pogo pins to eliminate poor electrical connection issues. Note that the top lid is missing in this picture to fully show the substrate in the assembly.

All the files necessary for the construction of this setup can be found in the public repository located in the link below, or by scanning the QR code from figure 1.12:

https://github.com/minusmagis/Nanopto_Hot_n_Cold_PCB

1.4.2 Software and Operation

As we have seen in the previous section, the temperature control circuit board can be operated with two digital signals, that can be controlled directly from the Pika demultiplexer’s Arduino nano. Two of the Arduino pins are connected to the “+/-” and “PWM” pins on the circuit

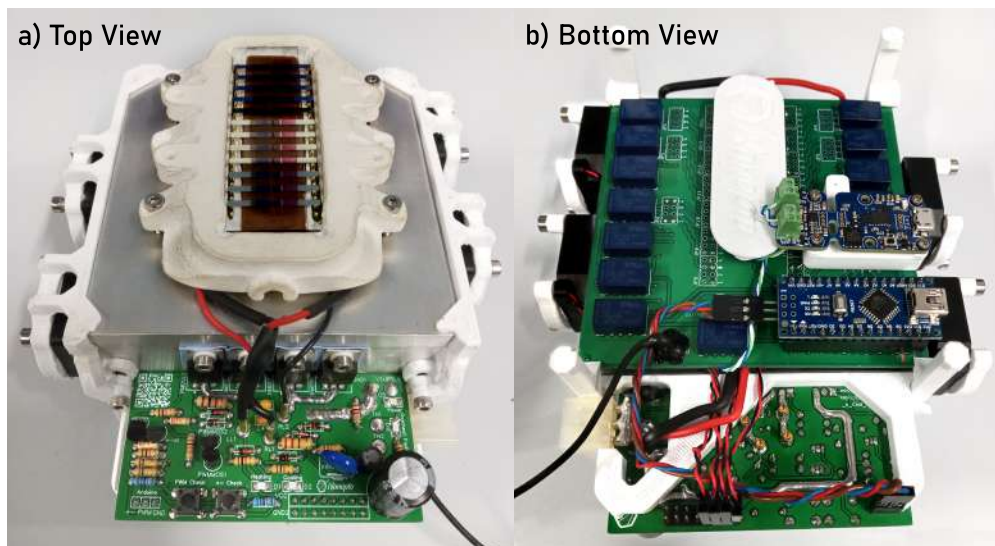


Figure 1.11: Pictures of the finished “Hot n’ cold” setup both from a top view (a) and a bottom view (b).



Figure 1.12: QR code to access the repository with all files related to the fabrication of the “Hot n’ Cold” setup.

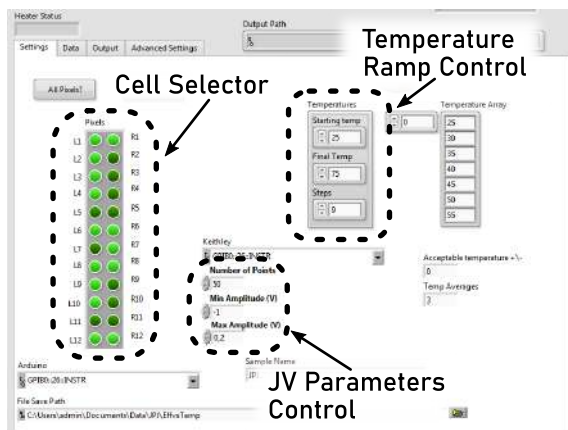


Figure 1.13: Graphical user interface front view of the control software that operates the entire “Hot n’ cold” setup, controlling the temperature and the JV measurements simultaneously.

board, which control current direction and power level respectively. Besides that, we needed to slightly modify the Arduino Pika demultiplexer firmware to control these two extra pins. This small modification consisted on the addition of a new command, through which we can control if we heat up or cool down, and with how much power. This command is composed by a letter, which can be either “*H*” or “*C*” for hot and cold, and a number with 3 digits from 000 to 255 that indicates the duty cycle of the PWM signal, effectively the amount of power the thermoelectrics receive for the selected mode. For example, if we sent the command “*H125*”, the Arduino would understand that it needs to heat the substrate, at half of the maximum power, so it would set the “+/-” pin to heating and it would send a PWM signal with a 50% duty cycle to the “PWM” pin.

The Pika demultiplexer board and the Yocto-thermocouple are connected through a LabVIEW script written by Dr. Jurado (figure 1.13), where, by polling the temperature and actuating the thermoelectrics in a closed feedback loop, we are able to finely control the temperature of our substrate within $<1^{\circ}\text{C}$ without overshooting. Besides, this software takes care of all the JV measurements at different temperatures as well as all the data processing and file saving. The user just needs to specify the temperature ramp parameters, as well as the JV parameters, and the software performs a temperature sweep, stopping at every specified temperature step and

performing a JV curve for each of the cells as fast as possible.

With the finished setup up and running we were fully prepared to study the performance of a wide variety of organic solar cells as a function of temperature.

1.5 Photoactive Materials Screening

In order to evaluate if there was a general trend in temperature dependent performance, we manufactured and characterized several solar cells with a variety of active layer materials to evaluate their behaviour at different temperatures. The results are summarized in figure 1.14, where we have separated materials into 3 groups according to their behaviour with temperature, which are: materials with **non-reversible decreasing** performance with increasing temperature (figure 1.14 (a)); materials with **reversible decreasing** performance with temperature (figure 1.14 (b)); and materials with **reversible increasing** performance with temperature (figure 1.14 (c)).

The photoactive materials from the first group (figure 1.14 (a)) are the ones that undergo some kind of degradation or performance decrease with thermal cycling, namely PBDBT-2Cl:ITIC-4F, PBDBT-2Cl:Y6 and PBDBT:PC71BM. For the PBDBT:PC71BM and PBDBT-2Cl:Y6 systems, performance stabilizes after the first temperature cycle removing any temperature dependence after having lost a 33% efficiency for PBDBT:PC71BM and a 15% for PBDBT-2Cl:Y6. It is a well known fact that PCBM tends to crystallize out of the active layer blend and form dimers at high temperatures, which has been reported to severely affect solar cell performance, which could explain this behaviour on the highest part of the temperature range, especially for unannealed samples.^{54,61} In the case of PBDBT-2Cl:Y6, we see that the efficiency does not immediately drop, but at higher temperatures performance starts to decrease, while for the case of PBDBT-2Cl:ITIC-4F, the degradation was constant and it did not stop after the first heat cycle. The remarked permanent performance decrease of these two polymers at

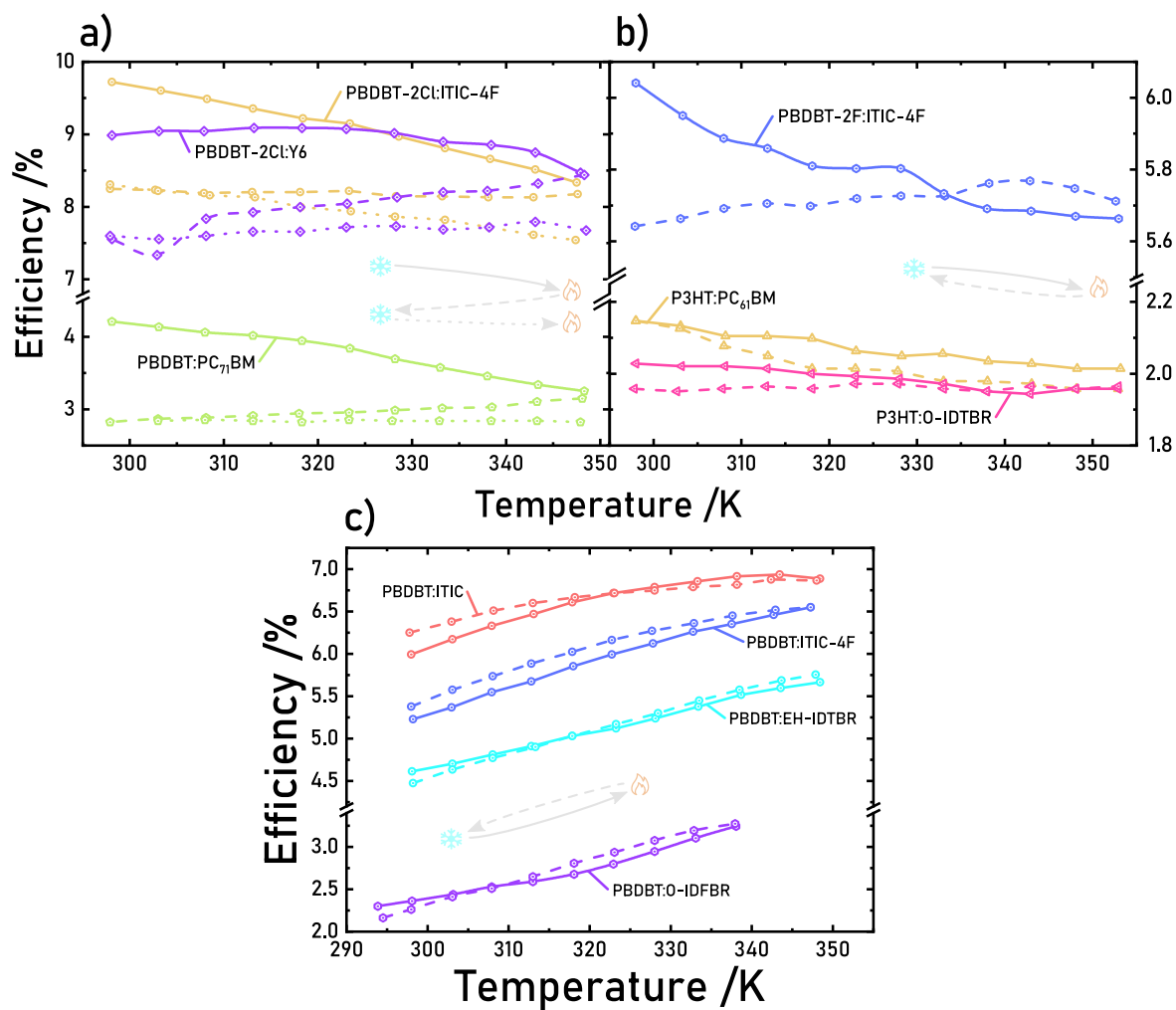


Figure 1.14: PCE evolution as a function of temperature and temperature cycling for different active layer materials that exhibit (a) permanent PCE decrease, (b) reversible PCE decrease, and (c) reversible PCE increase.

higher temperatures could be related to their lower crystalline packing when compared to their non-halogenated and fluorinated counterparts.⁸⁹

In the second material group, we find P3HT based systems (figure 1.14 (b)), which do not exhibit any performance increase at higher temperatures, rather the opposite. Their performance is slightly inferior at higher temperatures, changing in an approximately reversible manner with a negligible change in performance for P3HT:PC61BM and less than a 4% decrease for P3HT:O-IDTBR. We attribute this temperature stability to the fact that these active layer materials are annealed during their fabrication, at 135°C and 120°C for P3HT:PC61BM and P3HT:O-IDTBR respectively, greatly stabilizing their active layer morphology.⁹⁰⁻⁹² This stabilization has been previously reported in the literature where polymer blends exhibited a "temperature memory effect".⁹³ Alongside these two materials we bundled the results of devices based on a PBDBT-2F-ITIC:4F active layer, which also show a stable behaviour after temperature cycling, especially taking into account the lack of any annealing step during its manufacturing. Nevertheless, this material does exhibit a downwards trend with a PCE reduction of around 6% after the first temperature cycle. The higher temperature stability of fluorinated PBDBT blends, as opposed to chlorinated ones, has been previously related to their higher crystalline packing, making them inherently more stable at higher temperatures.⁸⁹

Finally, the third group exhibits a highly reversible behaviour with an increased PCE at higher temperatures, which englobes the systems based on PBDBT as a donor and either of the following acceptors: ITIC; ITIC-4F; EH-IDTBR; and O-IDFBR. This reversible enhancement in performance is generalized for every different acceptor within this material group, ranging from a 15% to a 42% increase (table 1.1). These blends also show some degree of irreversibility that, for blends containing ITIC or ITIC-4F, results in a slight permanent PCE increase, whereas for those containing EH-IDTBR or O-IDFBR leads to a small permanent performance drop. This irreversibility behaviour of ITIC blends will be further explored in the next sections. Nonetheless, all these PBDBT based photoactive material blends show greater PCE at

Material Name	Reversible Change (%)	Irreversible Change (%)	Annealing
PBDBT-2Cl:Y6	-5.7	-15.9	no
PBDBT-2Cl:ITIC-4F	-14.3	-15.2	no
PBDBT:PC71BM	-22.8	-32.9	no
P3HT:O-IDTBR	-3.1	-3.5	yes
P3HT:PC61BM	-6.2	0.0	yes
PBDBT-2F:ITIC-4F	-6.6	-6.3	no
PBDBT:O-IDFBR	42.3	-6.0	no
PBDBT:ITIC-4F	25.2	2.8	no
PBDBT:ITIC	14.9	4.3	no
PBDBT:EH-IDTBR	24.7	-3.0	no

Table 1.1: Reversible and irreversible change coefficients calculated from the ratio between the initial and final efficiencies (Irreversible Change) after one thermal cycling and the efficiency ratio between the initial and the efficiency at the highest temperature (348 K) (Reversible Change).

higher temperatures, suggesting that this donor could be one of the main drivers for temperature related performance enhancement, since, of all materials tested, only those containing this polymer show a significant PCE enhancement at high temperatures.

As mentioned before, since active layers based on PBDBT:ITIC showed the best enhancement factors, a good thermal stability, as well as the highest overall PCE of the materials within the last group, we decided to focus our characterization efforts on this material in order to further understand this phenomenon.

1.5.1 Temperature Dependent Electrical Characterization

Further JV characterization of PBDBT:ITIC active layers with thickness gradients can be seen in figure 1.15, which shows the the behaviour of four JV curve parameters, namely PCE, Jsc, Voc and FF, at various temperatures, for a variety of different active layer thicknesses. These parameters are measured during the first temperature cycle for the heating part, from 298K to 348K, as well as for the cooling part of the cycle back to 298K.

The experimental results reveal a strong positive relation between temperature and PCE that also depends on the active layer thickness. There appears to be a general performance increase at higher temperatures, being much more pronounced for thicker active layer cells, with a 71% PCE increase for the thickest 290 nm cell, and more modest for thinner cells, with a PCE enhancement of around 9%, at the highest measured temperature of 348K. In thicker cells, this efficiency increase occurs much more markedly at lower temperatures, leveling off as temperatures rise, while thinner cells exhibit a similar behaviour but with a much more gentle slope, indicating a weaker temperature dependence (figure 1.15 (a)). This behaviour is mainly driven by the Jsc sharply rising with temperature and slowly leveling off, combined with a steadily increasing FF. When combined with the decreasing Voc, the sharp Jsc and FF rise is softened, resulting in a steady increase in PCE.

However, if we contrast the PCE at the beginning and at the end of the measurement, it is clear that it has permanently increased (by 23%) after the entire temperature cycle, indicating that there are some non reversible effects taking place on the solar cell that are permanently enhancing the PCE, which we will investigate in later sections.

Figure 1.15 (b) (bottom) shows that, for both phases of the temperature cycle, the Voc decreases monotonically with temperature, with a constant slope of around -1 mV K^{-1} , much lower than

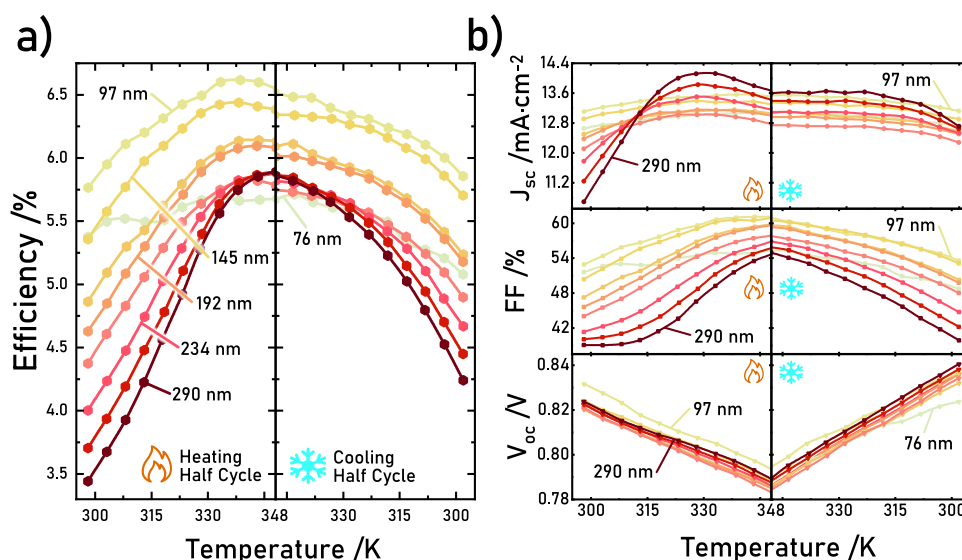


Figure 1.15: Temperature dependent parameters for a complete temperature cycle, of PB-DBT:ITIC based organic solar cells with different active layer thicknesses. Measured parameters are (a) PCE and (b) J_{sc} , FF and V_{oc} from top to bottom.

the one reported for silicon solar cells (-2.2 mV K^{-1}).¹⁸ This behaviour is in good agreement with reported literature, where it has been attributed to a shift in the quasi-Fermi levels of the photoactive material.^{94,95} Similarly to the PCE, after a complete temperature cycle the V_{oc} has been increased by 2.4% indicating some non-reversible behaviour that is permanently improving the V_{oc} of this device, albeit in a small amount.

On the other hand, there is a positive relation between the J_{sc} and temperature for every pixel thickness, where thicker active layers have a more pronounced response. Figure 1.15 (b) (top) shows that the slope of the curve is steeper for thicker cells at lower temperatures, leveling off as temperature rises until, only for the thickest cells, the trend seems to reverse after 340 K. The results of Figure 1.15 (b) (top) would agree with the above stated hypothesis where, at higher temperatures, charge mobility would be enhanced, resulting in a higher J_{sc} . In accordance with the hypothesis, this effect would be more pronounced for thicker cells, where charge mobility plays a much more critical role on the overall performance.

In this same figure we can see that the major driver of the PCE's non-reversible behaviour is a permanent increase in the J_{sc} after the temperature cycle of 26%. This permanent increase in J_{sc} could indicate a morphological change, which could be increasing charge mobility within the active layer, as we will see in later sections. Even with this permanent enhancement, the J_{sc} still exhibits a positive relation with temperature, with a reversible performance increase of 8% and an average slope of $17.2 \mu A K^{-1}$.

Finally, in figure 1.15 (b) (middle), the FF shows a positive relation with temperature, along the entire temperature range, with an enhancement of 40% at the highest measured temperature of 348 K and an average slope of $0.3\% K^{-1}$. This significant enhancement, which is highly reversible, seems to be the main driving factor of reversible PCE increase, alongside the smaller J_{sc} contribution. This positive relation is present for all thicknesses, again being more pronounced for thicker active layers. Upon closer examination, the latter show a small slope dip at lower temperatures in the first heating half cycle, which is not present in the following cooling half cycle. This fact suggests a possible non-reversible morphological transformation occurring at these temperatures, which prevented the fill factor from immediately rising, as opposed to thinner devices, where the FF starts to rise immediately. The fact that this dip is present only for thicker cells, at temperatures where their J_{sc} drastically increased, and that it disappears for the cooling cycle suggests that it is caused by the non-reversible behaviour of the cell on the first heat cycle, which could be related to an initial burn in.⁹⁶ However, an initial burn in would not be in agreement with the initial sudden rise in J_{sc} .

In order to visualize the temperature performance dependency at different thickness, and to compare with the following simulation results, we plotted the previous data with active layer thickness in the X axis, providing us with a different way to visualize obtained results (figure 1.16). These graphs make more apparent the stronger dependence between temperature and thickness, as well as the differences between the performance enhancement in the heating

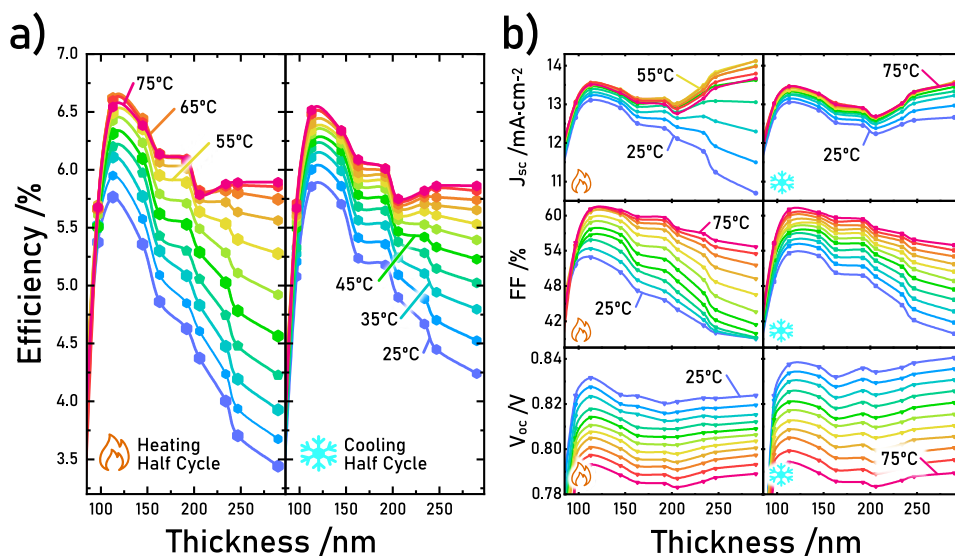


Figure 1.16: Temperature dependent parameters for a complete temperature cycle from figure 1.15, plotted using active layer thickness as the X axis. Measured parameters are (a) PCE and (b) J_{sc} , FF and V_{oc} from top to bottom.

and cooling half cycles. This figure also remarks the strong dependence of the fill factor with thickness, as well as the relatively invariant V_{oc} at different active layer thicknesses.

1.5.2 Further Characterization

Grazing Incidence X-Ray Scattering Characterization

The irreversible behaviours of both the J_{sc} and the V_{oc} during the first heating half cycle suggested a change in active layer morphology, which could explain the permanent PCE enhancement after the first temperature cycle. In order to evaluate any changes in active layer morphology we prepared several layers of PBDBT:ITIC, which were analysed using GIWAXS and GISAXS by Dr. Edgar Gutierrez and Dr. Jaime Martín. These techniques are specially oriented towards the characterization of surface thin film morphology, as explained in chapter ???. By measuring the samples before and after annealing the active layers, at 90°C for 10 min, they evaluated if there was any significant transformation in the morphology, while obtaining

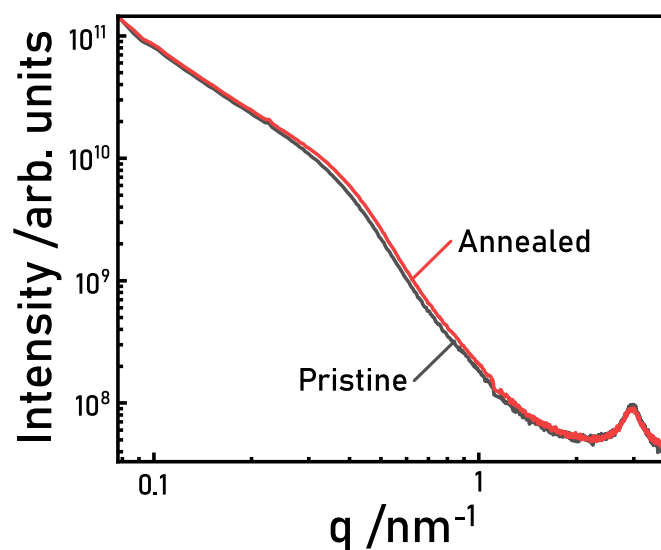


Figure 1.17: GISAXS spectrum for pristine and annealed PBDBT:ITIC thin films.

insight on the type of transformation.

The GISAXS spectra of the pristine and annealed sample (figure 1.17) show no difference in the present diffraction peak position or their general intensity. Nevertheless, we can see a slight general increase in the scattering intensity for the annealed sample. The GIWAXS spectra further confirm the lack of any major morphological change after annealing the samples, since the resulting scattering maps are practically identical (figure 1.18 (a)). To perform a more quantitative evaluation, Dr. Edgar Gutierrez integrated the GIWAXS spectra into two curves, in plane ($>45^\circ$) and out of plane ($<45^\circ$) (figure 1.18 (b)), where we again see that the major peaks do not change significantly neither in position nor in intensity, and the only difference we observe is a slight increase in the overall scattering intensity.

These results confirm there is no major change in active layer morphology at such low temperatures, which are significantly below the T_g of the active layer blend, around 470 K.^{97,98} The slightly raised scattering intensity, however, could be explained by the fact that ITIC blends can undergo diffusion limited crystallization well below their T_g .⁹⁷⁻⁹⁹ During this recrystallization

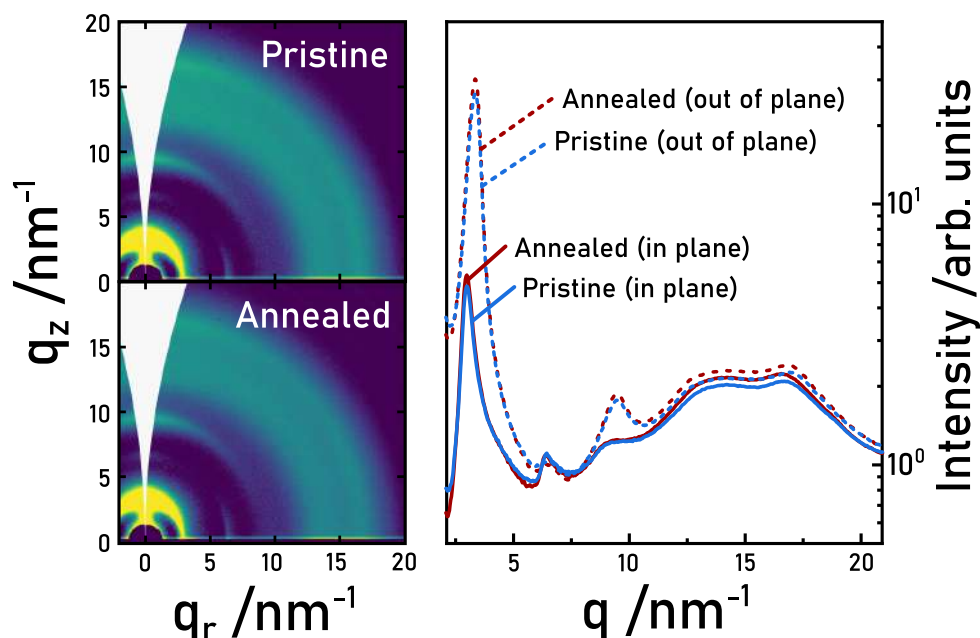


Figure 1.18: GIWAXS intensity maps for pristine and annealed PBDBT:ITIC thin films (left). Integrated GIWAXS spectra for the same films in two components: in plane ($>45^\circ$); and out of plane ($<45^\circ$)

process, which does not significantly change the overall crystalline structure of the film, ITIC crystalline domains become slightly larger, increasing phase separation in the active layer and thermally stabilizing the device. This low-temperature induced non-reversible phase separation has been associated to an increase in performance in previously reported literature.^{98,100,101} A slight enlargement of ITIC crystalline domains could explain the raised scattering intensity, without any major diffraction peak changes, as well as the irreversible increase in J_{sc} in the first heating half cycle. These bigger ITIC domains provide enhanced charge mobilities that result in a significant performance enhancement.¹⁰¹

Drift Diffusion Simulations

Parallelly, Dr. Mohammed Azzouzi simulated the electrical behaviour of our PBDBT:ITIC solar cells by using the drift diffusion model, to evaluate the role of recombination and charge

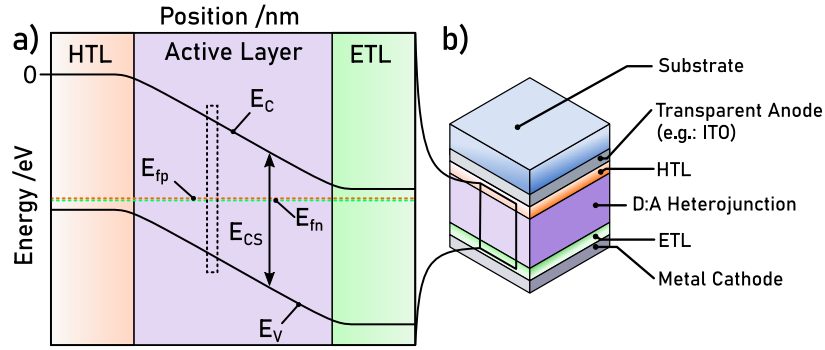


Figure 1.19: Device model considered in the paper. (a) Representation of a bulk heterojunction organic solar cell device, representing the different layers of the device stack. (b) Energy level diagram representation of the device. Figure adapted with explicit permission from the work of Azzouzi et al.²

mobility as a function of temperature. These simulations assumed a p-i-n band structure, with the active layer as the intrinsic layer, and the p and n layers as the HTL and ETL respectively (figure 1.19). This layer stack was assumed to have no series resistance and perfectly Ohmic contacts, as well as equal electron and hole mobilities with non-geminate recombination as the main recombination mechanism.

Two parameters were studied as a function of temperature: the charge carrier mobility; and the non-geminate pair rate formation, which is directly related to the recombination rate. To model these parameters we use equations 1.2 and 1.3 which describe the behaviour of charge mobility and non-geminate pair formation according to previously reported literature.^{2,102}

$$\mu(T) = \mu_{300K} e^{\left(\frac{E_{a,\mu}}{k_b} \left(\frac{1}{300K} + \frac{1}{T}\right)\right)} \quad (1.2)$$

Equation 1.2 describes the dependence of charge mobility with temperature, where μ is the charge mobility, $E_{a,\mu}$ is the charge carrier mobility activation energy, T is the device temperature and k_b is the Boltzmann constant. μ_{300} was set to $2 \times 10^{-4} \text{ cm}^2 \text{ V}^{-1} \text{ s}^{-1}$, which is a typical

value for this active layer blend.¹⁰³

The next equation (1.3) describes the temperature dependence of the non-geminate pair formation from free charges, which is directly related with the recombination rate:

$$k_{for}(T) = k_{for(300K)} e^{\left(\frac{E_{a,k_{for}}}{k_b} \left(\frac{1}{300K} + \frac{1}{T}\right)\right)} \quad (1.3)$$

Where k_{for} is the rate of non-geminate pair formation, $E_{a,k_{for}}$ is the non-geminate pair formation activation energy, T is the device temperature and k_b is the Boltzmann constant. k_{for} was set to $1 \times 10^{-11} \text{ cm}^3 \text{ s}^{-1}$, which, according to previous studies, is a realistic estimation for this coefficient.²

Having two variable parameters, the most logical approach was to simulate four main cases, two where each of the activation energies would be separately evaluated as a function of temperature, one where they are both simultaneously dependent on temperature, and the trivial solution. This trivial solution case, which was the first to be simulated, was the one where the two variables are completely temperature independent, assessing the most fundamental changes when there is no change in mobility or recombination with temperature.

This simulation case (figure 1.20) shows a Voc decrease at higher temperatures for all active layer thicknesses, similarly to the Jsc of the thinner devices. The FF and the Jsc of thick devices, on the other hand, show a moderate increase until the middle of the temperature range, where the trend reverses bringing them down to the starting values at higher temperatures. Combining these three simulated values, the resulting efficiency decreases at higher temperatures for all active layer thicknesses, rendering a simulation that does not resemble our experimental results, with the exception of the Voc, which shows a similar trend.

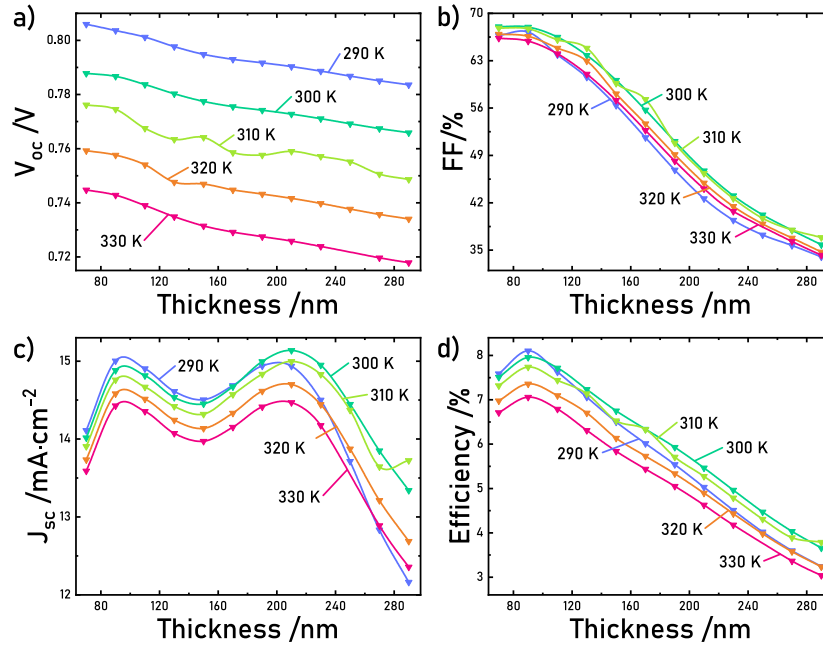


Figure 1.20: Drift diffusion simulation results, (a) V_{oc} , (b) FF, (c) J_{sc} and (d) efficiency, for temperature independent recombination rates and charge mobility ($E_{a,k_{for}} = 0$ and $E_{a\mu} = 0$).

In the second case (figure 1.21), we evaluate the recombination rate in isolation, by setting $E_{a,k_{for}}$ to 0.4, while keeping charge mobility independent from temperature. In this simulation the V_{oc} behaves in a similar manner as in the previous simulation, decreasing with temperature. At room temperature, this V_{oc} is slightly lower than in the previous case, but it seems to be less affected by high temperatures, where its decrease is slightly less pronounced.¹⁰⁴ Contrarily, the FF and the J_{sc} are severely affected by the increased recombination at higher temperatures, being significantly lower for every active layer thickness. This fact agrees with our hypothesis and previously reported literature, where higher recombination rates will result in a competition between charge extraction and charge recombination, lowering the J_{sc} and the FF through a lower R_{sh} .⁷⁶ Nonetheless, this results in a decreasing efficiency at higher temperatures, which is still not in accordance with our experimental measurements, with the exception of the V_{oc} .

In the third case we simulate the opposite scenario, where charge mobility dependence with temperature is evaluated in isolation. For this, we set $E_{a,\mu}$ to 0.4, resulting in a mobility change

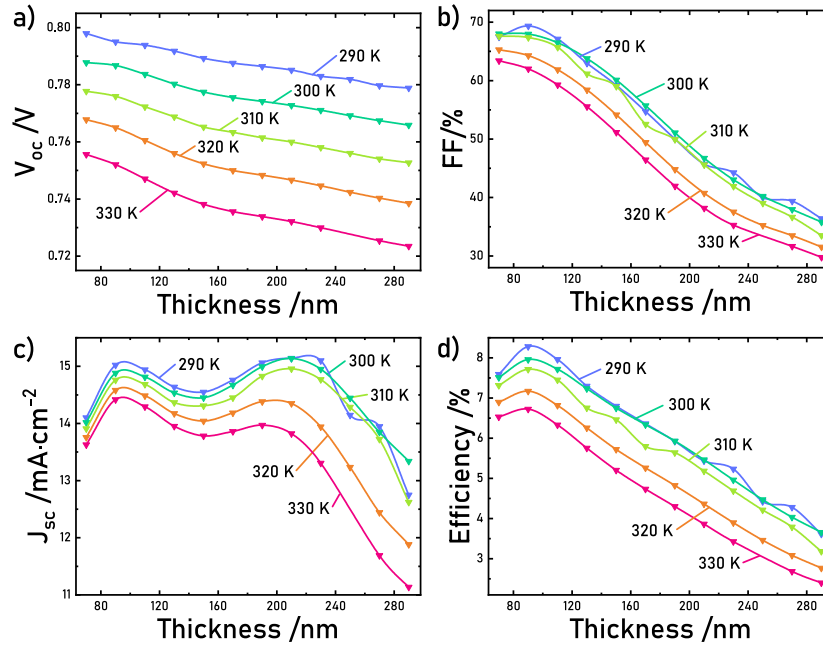


Figure 1.21: Drift diffusion simulation results, (a) V_{oc} , (b) FF, (c) J_{sc} and (d) efficiency, for temperature dependent recombination rates and temperature independent charge mobility ($E_{a,k_{for}} = 0.4$ and $E_{a\mu} = 0$).

of an order of magnitude (from $2 \times 10^{-4} \text{ cm}^2 \text{ V}^{-1} \text{ s}^{-1}$ to $2 \times 10^{-3} \text{ cm}^2 \text{ V}^{-1} \text{ s}^{-1}$) along the 300 K - 350 K range, with a temperature independent recombination rate. In this case, the V_{oc} behaves exactly as it did in the first simulation, decreasing monotonically with temperature, independently of active layer thickness. The FF exhibits a general increase at higher temperatures, being more pronounced on thicker cells, confirming that with higher mobilities and the same charge recombination coefficient, the resulting higher charge extraction will increase the FF. This effect is even more pronounced for the J_{sc} , exhibiting a drastic increase at higher temperatures for thicker active layers where lower charge mobilities hinder charge extraction.¹⁰⁵ On thinner active layers, where charge extraction is not a limiting factor, the fundamental decrease in J_{sc} seen in previous simulations dominates, resulting in a lower performance at higher temperatures. The resulting efficiency is higher at higher temperatures for every active layer thickness, with thicker layers exhibiting the greatest improvements. These simulation case is in good agreement with our experimental results, strengthening the hypothesis that the temperature dependence of charge mobility is one of the major drivers for performance enhancement.

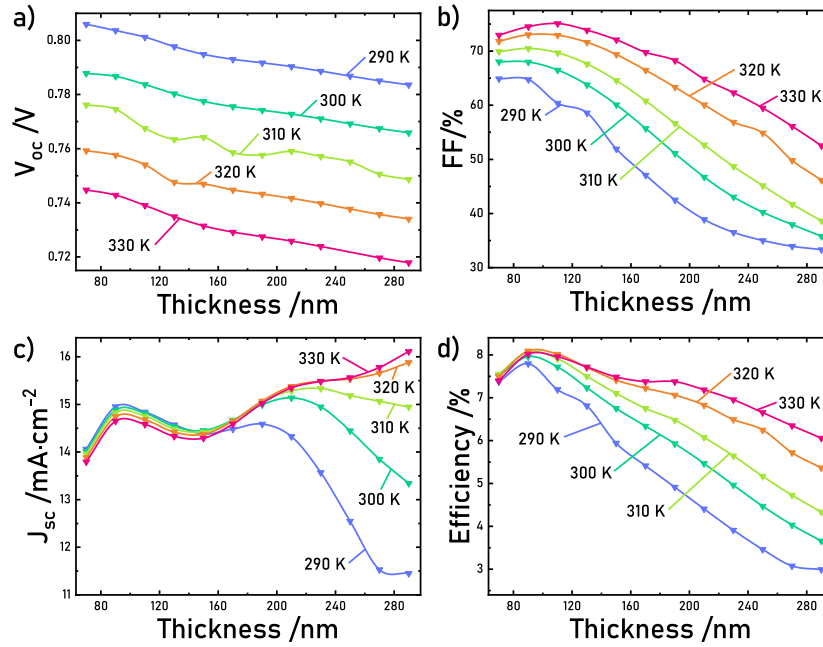


Figure 1.22: Drift diffusion simulation results, (a) V_{oc} , (b) FF, (c) J_{sc} and (d) efficiency, for temperature independent recombination rates and temperature dependent charge mobility ($E_{a,k_{for}} = 0$ and $E_{a\mu} = 0.4$).

In the final case, the two previous cases were combined to evaluate any synergistic interaction they might have, by simulating a temperature dependence of both charge mobility and recombination rate in the same system. The V_{oc} behaves very similarly to previous simulations, closely resembling that of the second case, but with a stronger dependence on temperature. Similarly, the behaviour of J_{sc} and FF greatly resembles that of case 3, where the FF was enhanced for every thickness, and J_{sc} was only increased for thicker cells. The main difference is that the FF enhancement is less pronounced with temperature, fact that results from combining the second and the third simulation case, where higher recombination rates compete with higher charge mobility at higher temperatures. In this case, however, charge mobility enhancement overruns the increased recombination, resulting in a higher FF at higher temperatures. This is translated in a higher efficiency at higher temperatures for every active layer thickness, with thicker layers exhibiting the greatest improvement, but with a lower absolute improvement due

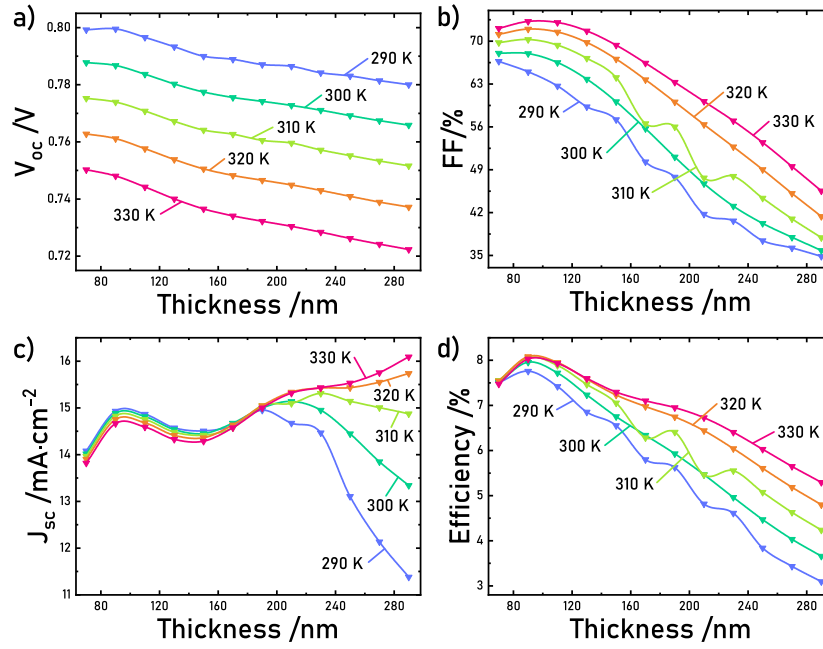


Figure 1.23: Drift diffusion simulation results, (a) V_{oc} , (b) FF, (c) J_{sc} and (d) efficiency, for temperature dependent recombination rates and charge mobility ($E_{a,k_{for}} = 0.4$ and $E_{a\mu} = 0.4$).

to the lower FF increase at higher temperatures. These results are still in good agreement with our experimental data, however, the enhancement we see on the FF is lower than that of our experimental results.

These two last simulation results are in good agreement with the experimental results reported in the previous section, with a constantly decreasing voltage and generally higher J_{sc} and FF at higher temperatures, especially pronounced in thicker layers. Comparing them quantitatively, we see that the V_{oc} is generally lower in the simulations, but the simulated temperature dependence is really close to that of our experimental data, with a slope of -1.15 mV K^{-1} for the simulations and -1.0 mV K^{-1} for real devices. Besides, the V_{oc} shows a much stronger dependence with thickness in the simulations, as opposed to that of real devices.

J_{sc} values are similar as well, being higher overall in the simulations, with the exception that,

in the simulations, higher temperatures are always detrimental for thinner active layers, while real devices exhibit an increased J_{sc} at all active layer thicknesses, even the thinnest ones. J_{sc} enhancements however, are significantly higher for the simulations, especially for thicker solar cells.

Similarly to the case of the V_{oc} , the FF exhibits a stronger dependence with thickness for simulated devices than for real ones, with a lower FF for thicker active layers and a higher FF for thinner layers than those reported in our previous experiments. The temperature dependence of the FF in simulation case 4 closely matches that of real experimental data, with a 24.5% enhancement ratio for the thickest active layers, in both simulated and real devices. The exaggerated dependence between the FF and active layer thickness is reflected in the efficiency, where, comparing the simulations with the experimental data, we see that simulated thin devices exhibit higher efficiencies than real thin devices, whereas thick simulated devices perform much worse than their real counterparts. This can be related to the fact that we have assumed the donor acceptor interface as an intrinsic region where the field is mainly set by the CTLs, while in reality this region is a BHJ, with a much stronger electric field in the donor-acceptor interface which is less affected by changes in device thickness. Nevertheless, the general behaviour of this parameter is in good agreement with experimental data, wherein the efficiency is higher at higher temperatures for every active layer thickness, with this effect being more pronounced for thicker devices.

The latter simulations are in good accordance with the experimental results, strengthening the hypothesis that charge mobility enhancement at higher temperatures is one of the major drivers of the reversible PCE enhancement. These results suggest that the raise in recombination rate within this temperature range and the decreased V_{oc} are not sufficient to overshadow the charge mobility enhancement which drives FF and J_{sc} up.

For further comparison between the different simulation results, we have assembled a figure that summarizes them into a very compact and understandable way, which can be found in the appendix of this chapter.

EQE and Mobility Measurements

As an expansion of this work, Dr. Jurado performed several additional measurements in order to gain further insight into the temperature dependent performance of PBDBT:ITIC organic solar cells, some of which have been included in this section for the sake of completeness.

Firstly, upon measuring the dependence of the EQE curves with temperature, we see that, similarly to previous experimental results, thicker active layers exhibit a higher temperature dependent performance (figure 1.24). By measuring the EQE of these cells after the first heating cycle, to remove any irreversible effect, we see that the EQE is mainly increased closer to the band gap, while there is barely an enhancement around shorter wavelengths. At first, we attributed this phenomenon to the fact that, the absorption of photons with smaller wavelengths, results in higher energy charge carriers (hot carriers), which are promoted to lower occupation levels, reaching the contacts faster. However, the ultra-fast charge thermalization times of few nanoseconds reported in the literature made us discard this hypothesis.^{106,107} Another hypothesis that might explain this phenomenon is related to the charge separation efficiency, which could be higher for hot carriers, since these have more energy to escape Coulombic attractions. Previously reported literature seems to point towards the same direction, but without any definitive answer yet.^{108,109}

In our opinion, the most plausible hypothesis is that, this behaviour arises from an uneven charge generation across a thick active layer. As we have seen in chapter ?? [??ch:4 Photonics on OPV: Nanostructured NIR Photodetectors: Introduction], the hindered performance of thicker active layers, on the regions where the photoactive materials have a high absorbance, can be explained by charge collection narrowing. This phenomenon is characterized by a higher

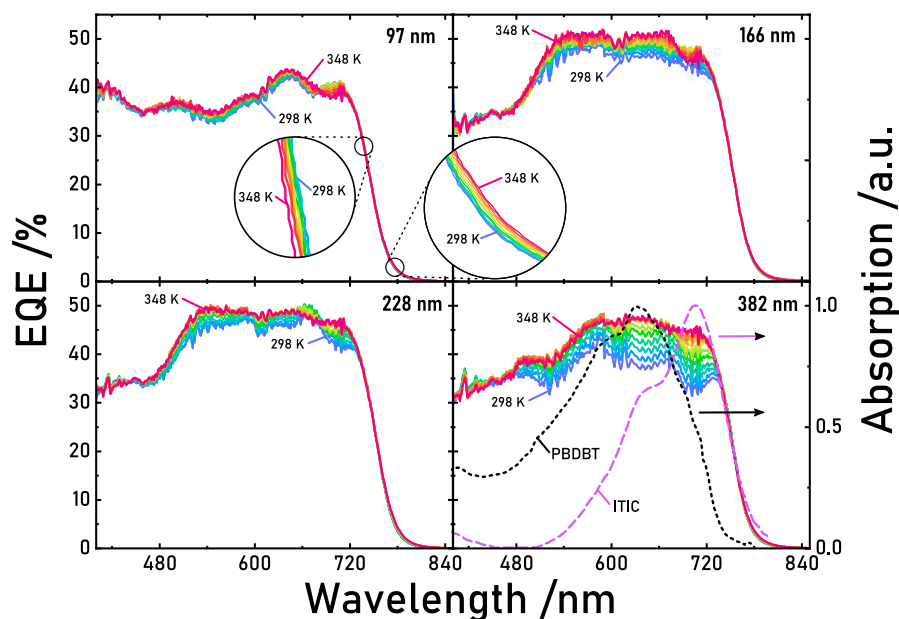


Figure 1.24: EQE curves for four different active layer thicknesses of PBDBT:ITIC based organic solar cells taken at different temperatures ranging from 298 K to 348 K.

charge generation in the active layer region closer to the front transparent electrode, where most of the light is absorbed. This uneven charge generation distribution across the active layer, combined with a high thickness, results in lower charge extraction. Nonetheless, by raising the temperature and increasing charge mobility, charges generated on one side of the active layer have a higher probability of reaching the other side. That is why, by heating the active layer, charges generated with highly absorbed wavelengths will have a higher chance of reaching the back electrode, resulting on an increased EQE within that wavelength range. We can clearly see that the wavelength dependency of this enhancement is strongly related with the absorption of the blend, because charges generated by the poorly absorbed UV-Blue regions, which are more evenly absorbed throughout the active layer, are less affected by an increase in charge mobility (figure 1.24). For a more in depth explanation of this phenomenon the reader is referred to appendix??: ??ch:4 Photonics on OPV: Appendix: Active Layer Thickness],

Even though the EQE values change in intensity at different temperatures, the lack of major peak changes in the EQE curves in figure 1.24 indicates that, EQE enhancement at higher

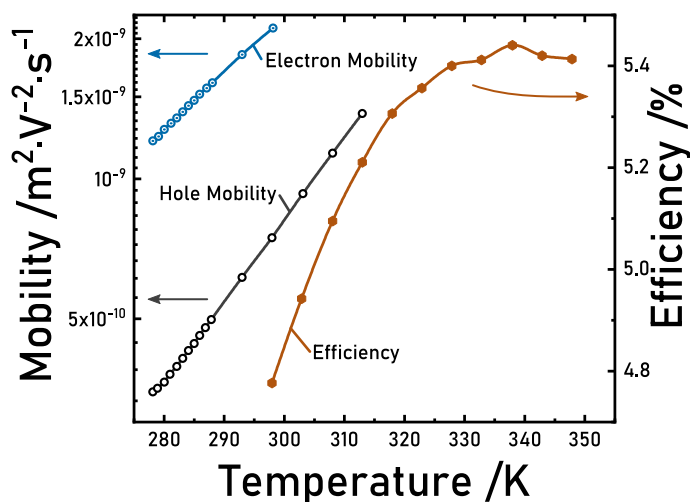


Figure 1.25: SCLC fit results with electron and hole mobilities for PDBDT:ITIC based electron and hole only devices with an active layer thickness of 160 nm side by side with the efficiency of a similar thickness device (163 nm).

temperatures is not related to morphological changes. Such changes typically result in major deformation of the EQE curve, with a certain degree of unequal peak intensity changes and/or slight band gap shifting, induced by changes in the crystalline structure and/or phase separation, which are present for all active layer thicknesses.^{38,110,111} In that same figure, we can see how the EQE tail tends to flatten at higher temperatures for all thicknesses. We have zoomed on the curve of 97 nm as an example, but this trend is general for the four active layer thicknesses. This behaviour can be explained by phonon-electron coupling that results in a slight red shift and a broadening of the absorption for many materials, which are described by semi-empirical relationships based on a Bose-Einstein phonon distribution.^{24,112–115} This is related to the energy lowering of the quasi-Fermi levels, in agreement with the lower V_{oc} at higher temperatures that we saw on the experimental results.

These results reveal that the spectral response of a solar cell can be varied by controlling the active layer temperature. This is an interesting fact because it confirms that we can increase the performance of a solar cell by heating it up, but, on a different note, it opens the possibility to moderately regulate the spectral responsivity of OPV devices by accurately controlling their temperature, which can be interesting in other OPV fields such as in organic photodetectors.

Measuring the mobilities of our active layer blend at different temperatures was the only missing piece of this entire work. For that, Dr. Jurado manufactured electron only and hole only devices, where both charge transport layers are either ETL or HTL, and characterized them by performing SCLC fits to extract the charge mobility from the measurements. The models used to extract mobility parameters and a detailed explanation of SCLC regime can be found on previously reported literature by Felekidis et al.¹¹⁶ and Blakesley et al.¹¹⁷ For a correct charge mobility calculation, the measurements were performed at lower temperature ranges (278-313 K), where the voltage region with completely filled traps was easily identifiable.

The fitting results can be seen in figure 1.25, where both electron and hole mobility, even though showing different values, significantly increase with temperature for a PBDBT:ITIC active layer. This increase in charge mobility is in good agreement with the results of previous sections, where the FF and the Jsc were improved at higher temperatures, ultimately leading to higher PCE at higher temperatures (figure 1.25 (brown line)).

1.5.3 Conclusions

In this chapter we have manufactured a fully functional temperature adjustable solar cell measuring setup. This setup, named “Hot n’ cold”, is able to subject pre-scale up solar cells to temperatures from 273 K to 363 K ($\sim 0-90^{\circ}\text{C}$) with temperature ramps of up to 5 K s^{-1} . At any given temperature it can connect to all the solar cells within the substrate by means of a relay based multiplexer, that allows for a high speed measurement of the entire substrate. Besides, it is a fully open source setup, easy to manufacture in any lab that requires it, without the need of specialized tools or knowledge, by outsourcing some of the most difficult processes.

With this setup, we have studied the temperature dependence of a variety of organic solar cell materials, which exhibited three main behaviours upon thermal cycling: **permanent per-**

formance decrease with increasing temperatures; **reversible performance decrease** with temperature; and **reversible performance increase** with temperature. Within the latter material group, we decided to focus on PBDBT:ITIC blends, since they exhibited the greatest absolute performance, along with a great thermal stability and high temperature dependent PCE enhancements.

We showed that thermally cycling PBDBT:ITIC blends results in both an irreversible and reversible PCE enhancement. The overall enhancement is more pronounced in thicker active layers, with PCE improvements of up to 71% at 348 K, with 39% being reversible and 32% non-reversible. Both experimental measurements and drift diffusion model simulations, confirm that the reversible fraction of this enhancement can be attributed to an increased charge mobility in the active layer at higher temperatures, which is not overshadowed by the increase in recombination rate. On the other hand, GIWAXS and GISAXS experiments revealed no major changes on active layer morphology, which led to the conclusion that irreversible PCE enhancement is related to a small change in the size of ITIC crystalline domains, driven by low temperature phase separation, previously reported in the literature.^{97–99} Finally, EQE and SCLC measurements have confirmed an increase in the charge mobility at higher temperatures, related to higher light conversion efficiencies, especially pronounced in thicker active layers.

In summary, we have proven that by increasing the temperature of certain organic solar cells, more specifically those based on PBDBT, their performance is increased for any active layer thickness, with a stronger effect for thicker active layers. This result is really interesting for large scale roll-to-roll solar cell manufacturing, where thickness variations intrinsic to the manufacturing process, which lead to inconsistent module performance, can be even out by raising the module temperature allowing for wider manufacturing tolerances.¹¹⁸



Appendix

This appendix adds onto some of the calculations and optimization processes performed during the experiments described on this chapter. It also provides alternative representations that aid in the visualization of data presented in this chapter.

1.A Voc Calculations

An easier way to calculate the correct relationship between Voc and temperature theoretically, can be derived from the perspective of charge-carrier concentrations. With this point of view, the Voc is obtained from the difference in chemical potential between electrons and holes, here depicted as quasi-fermi levels (equation 1.4).^{94, 119}

$$qV_{oc} = E_{fn} - E_{fp} \quad (1.4)$$

In solar cells based on bulk silicon, free carrier density is described by Fermi statistics, which in this case can be approximated with a Boltzmann distribution, resulting in equation 1.5.⁹⁴

$$qV_{oc} = E_g - k_b T \ln \left(\frac{N_c N_v}{np} \right) \quad (1.5)$$

Where: E_g is the band gap energy; N_c and N_v are the effective conduction and valence band density of states; n and p are the free electron and hole concentrations; and k_bT is the thermal energy.

For organic materials, the trend is similar, exhibiting a negative temperature Voc coefficient around room temperature. These similarities arise from the fact that at high enough temperatures, charge carriers in organic semiconductors can also be modeled with a Boltzmann distribution, under low-occupancy conditions.⁹⁵ For organic solar cells in these conditions though, we need to add another term to equation 1.5, resulting in equation 1.6, to account for the equilibration energy (σ^2/k_bT), which for basic organic active layer blends such as P3HT:PC61BM is around 0.3 mV K⁻¹ at 300 K.⁹⁴ This term takes into account the Gaussian nature of the density of states in organic semiconductors, where, under low-occupancy conditions most carriers are distributed not around the Fermi level, but rather around the so called equilibration energy, with a Gaussian width σ .^{120,121}

$$qV_{oc} = E_g - \frac{\sigma_n^2 + \sigma_p^2}{2k_bT} - k_bT \ln \left(\frac{N_c N_v}{np} \right) \quad (1.6)$$

In that equation we see that the term that accounts for the equilibration energy, being split into hole and electron components, has a positive relation with temperature which can explain the smaller negative temperature coefficients reported in organic solar cells vs the ones in inorganic photovoltaics.⁹⁴ Experimentally it has been observed that the Voc follows this negative trend until, below a certain temperature, it levels off.¹²² This Voc saturation level has been observed to be lower in more ordered materials like bilayer heterojunctions.¹²³

This additional factor in equation 1.6 would explain the, previously reported, less aggressive decline of the Voc in OPV with increasing temperatures, when compared to inorganic PV technologies, which would result in less affected Voc values, allowing for enhanced efficiencies

at high temperatures.⁹⁴

1.B PLA Salt Remelting/Annealing

We chose to use plastic 3D printing in our prototyping process because it is a great technology that allows for the manufacturing of complex pieces in a matter of hours, in a completely customizable and really affordable process.¹²⁴ This enables us to run through many different designs quickly, being able to test them in real situations, until we find an optimized solution that fits our needs.

Most plastics, however, suffer from a phenomenon called creep, where they begin to yield and deform under constant pressure, a phenomenon that is magnified at high temperatures, especially above T_g .^{125,126} The main drawback of using 3D printing as our prototyping technique, is that most commonly available 3D print plastics have a glass transition temperature below 90°C, and those which don't are really expensive and rather difficult to 3D print.^{127–129} However, for the “Hot n’ cold” setup, we needed several pieces that would have to withstand these high temperatures for extended periods of time without deforming, and need to be electrically and thermally insulating, while being robust and lightweight. Polymeric materials were the perfect candidate.

Luckily, we found the solution to that problem in one of the most common 3D printer materials available: Poly Lactic Acid or PLA. Ironically, this polymer has one of the lowest glass transition temperatures of typical 3D printable plastics, around 60°C.^{130,131} Nevertheless, being a rather simple polymer chain, it can exhibit a high degree of crystallinity under the right cooling conditions.^{132,133} In a highly crystalline polymer the glass transition will slowly disappear, leaving only the melting phase change, significantly increasing this polymer's resistance to creep at high temperatures.¹²⁶ This means that highly crystalline PLA is able to withstand much higher

temperatures than any other commonly 3D printed plastic without permanent deformation.

The most common way to increase the crystallinity of PLA is to perform a thermal annealing, where we heat up above T_g so that the polymer chains can rearrange in a highly crystalline structure. The problem with annealing 3D prints is that, due to the nature of this technique, where plastic is rapidly cooled down after being molten, the resulting polymer matrix has a very low degree of crystallinity as well as a lot of accumulated stresses.¹³⁴ That means that during the annealing process, these uneven stresses greatly distort the original shape and the piece undergoes uneven elongation and shrinkage, compromising dimensional accuracy.¹³⁵

To solve this problem we decided to use PLA salt remelting/annealing, a technique previously reported in literature, which we further refined.^{136,137} This technique consists on fully surrounding a 3D print with finely ground salt, and heating it up just above the melting point, before slowly cooling it back down. This ensures that all the polymer chains are completely free, so that when they slowly solidify again, they have the ability to form big crystalline domains.¹³⁸

For this process to work, 3D printed pieces are printed completely solid, as opposed to most 3D printed pieces which are printed hollow, with some sprues to provide enough material during melting to compensate for the shrinkage natural to the process (figure 1.26 (left)). Since the printing process traps a lot of air within the structure, these sprues also serve as material reservoirs where all the air pockets rise up to, when they merge into a big bubble during the melting process (figure 1.26 (right)).¹³⁹ These sprues are easily snapped off with pliers after the part has cooled down.

It is very important that the salt is finely ground because, if tightly packed around the 3D printed piece, it will hold the shape even when the plastic is molten, providing a mold for the plastic to resolidify with the exact same shape as it had before melting, aside from preventing the PLA from diffusing into the salt matrix. The only drawback of this technique is that it leaves a rough surface as rough as the grains of salt used for the process (figure 1.27). The

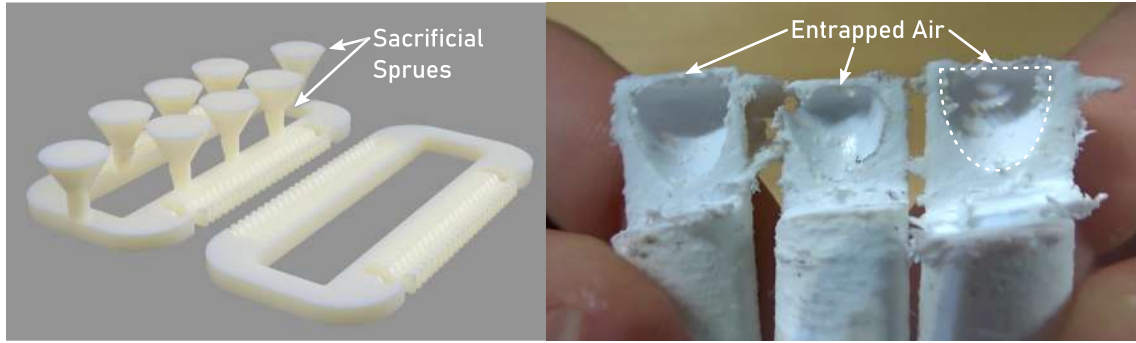


Figure 1.26: 3D render of the rib cage (6) without and with sprues added to prevent holes from forming during salt remelting (left). Cross section view of three cylindrical solid samples after salt remelting, showing a bubble formed during the salt remelting process, where all the air pockets entrapped during 3D printing have merged into one big bubble (right).



Figure 1.27: 3D printed piece after being remelted in rough grain salt. The surface of the piece becomes extremely rough and the dimensionality of the piece gets compromised due to the molten PLA flowing outwards into the intergranular space.

resulting pieces are not only temperature resistant up to $\sim 160^{\circ}\text{C}$, but they are completely solid, making them as strong as injection molded pieces.¹³⁷

We have tried to perform this experiment with similar packing materials, such as plaster, which should be able to more easily hold its shape. However, its high water content promotes hydrolysis of the polymer chains resulting in extremely fragile and brittle solid 3D prints.

Such highly crystalline PLA pieces can be easily machined (when compared to other plastics) to final tolerances, without the need for coolant thanks to its temperature stability. That is why, all the high temperature pieces that needed to interact with precisely machined parts,

such as the copper block and the pogo pins, where manually machined to perfectly fit with said pieces.

1.B.1 Circuit Design

In order to regulate the substrate temperature we need to be able to control the thermoelectric module's power by regulating how much current flows through the circuit, since heat pumping power is directly proportional to the amount of current passing through the thermoelectric modules.^{140,141} A common and really simple way to regulate this power is by using a voltage regulator. However, since we want to operate the thermoelectrics in both directions, besides controlling the power, we need to be able to reverse the current running through the modules. This requires the usage of, either two separate floating ground variable power supplies, or a much more simple, compact and inexpensive H bridge circuit.

This kind of circuits are usually used to control heavy loads that require current to be passed in both directions, usually DC motors, so it was a really good fit for our application. The main problem is that we need to switch the direction of a high current (tens of amps), while at the same time modulating this current flowing through the thermoelectrics, which requires the use of a really high power specialised H bridge circuit. However, since these circuits are usually specialized in DC motor driving, the most common ones cannot switch as much current as we'd like, being limited to 5-7 A, and they do not tend to provide power modulation. Because of that, we were not able to find a suitable commercial solution, so we decided to create our own high power power modulating H bridge circuit, with off the shelf components.

The main components of any H bridge are 4 switches that control the current flow, which are usually not mechanical switches, but electrically actuated ones called MOSFETs (figure 1.28 (a)). Nonetheless, to keep the explanation from getting too technical, they are depicted

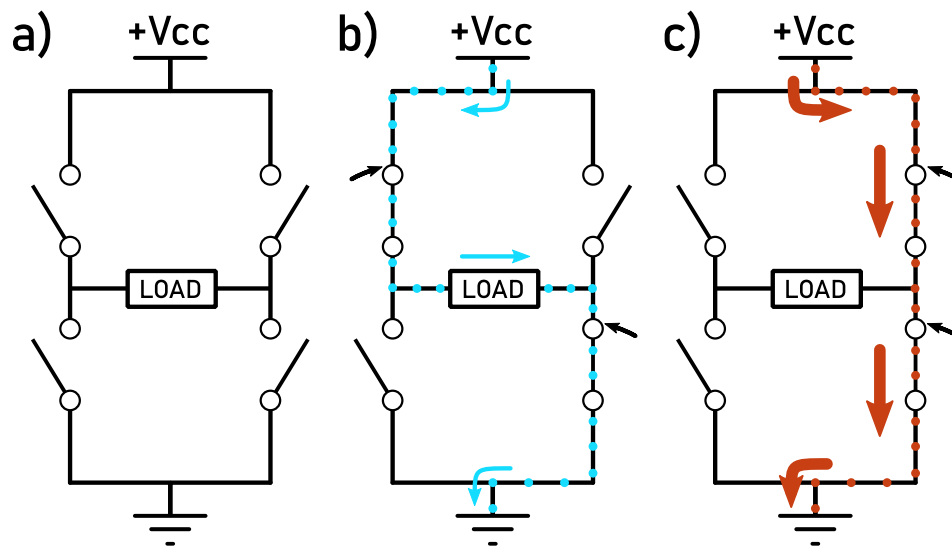


Figure 1.28: (a) H bridge conceptual schematics using 4 switches and one load. (b) Current flow during normal operation. (c) Current flow on short circuit condition.

in the figures with the symbol of a mechanical switch. These 4 MOSFETs operate in a cross like pattern where one of the diagonals will be open while the other will be closed, forcing current to flow through the load in one direction (figure 1.28 (b)). The entire point of the circuit is that, if we activate the switches in the opposite diagonal, the current will pass in reverse through the load, which will revert the heat pumping direction, effectively shifting the thermoelectric modules from heating to cooling or vice versa. However, if we were to operate these 4 MOSFETs independently, we can quickly see that there is a potentially catastrophic failure condition in this circuit, where both MOSFETs on a vertical branch are on at the same time, creating a short circuit (figure 1.28 (c)). To prevent that, we need to implement a logical control circuit around these four MOSFETs, so that this condition is impossible or at least highly improbable.

To solve that problem, we designed a control unit with several transistors that work as logic gates around the four main MOSFETs (figure 1.29 (a)). When combined, these logic gates enforce an electrical interlock that prevents any of the two MOSFETs within a same branch

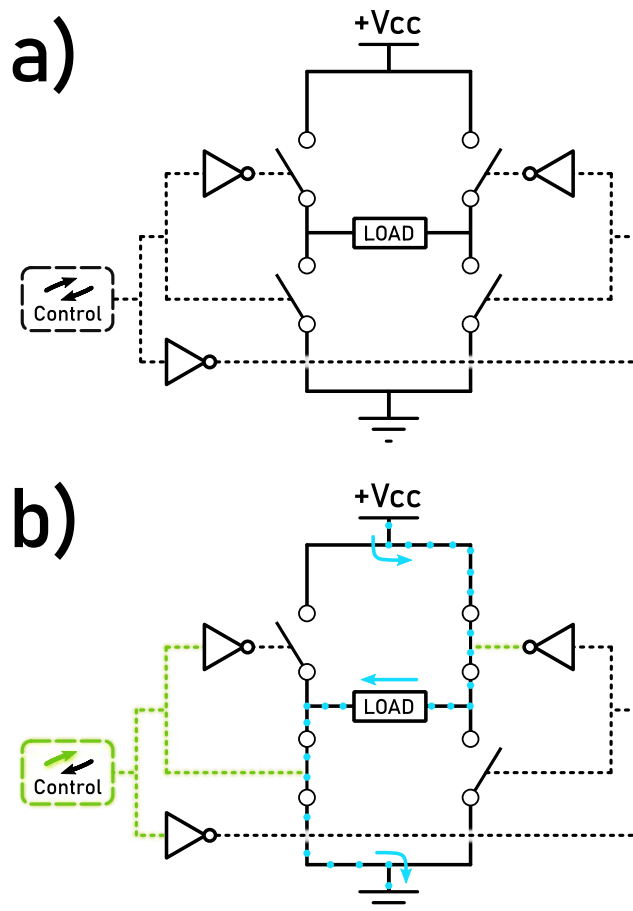


Figure 1.29: (a) H bridge conceptual schematics with current direction control circuit based on logic gates. (b) Current direction control circuit operating switches through the logic gates.

to be on at the same time. Being controlled by only one digital input, the entire logical circuit guarantees that only one MOSFET of each vertical branch will be closed at any time but never both, preventing any short circuit, while, at the same time, regulating the current direction through the thermoelectric modules (figure 1.29 (b)).

The most eagle eyed will have seen that, when reversing the current, there can be a brief moment where the two branches could be connected at the same time. In the time one of the MOSFET's gate takes to discharge, the other can get charged causing a short-circuit for a very brief period of time. This phenomenon can be mitigated either hardware-wise, by measuring MOSFET gate charging and discharging times and regulating their resistors, or software-wise, by not changing from cooling to heating in a rapid sequence. We chose to use the latter to keep the circuit as simple and robust as possible.

This simple H bridge circuit is able to either give full power in one direction, or in the other, effectively heating or cooling always at max power. Nonetheless, to provide accurate temperatures we need to modulate the power we provide to the thermoelectric modules, which can be easily achieved with digital PWM signals. These signals consist on a square wave with a fixed frequency and amplitude, where the ratio between the width of the high and low sections of the one single period of the signal, aka the duty cycle, is modulated. This modulation determines the time fraction where the load will be receiving power during one wave period. For example, for a 20% duty cycle signal, the signal is high 20% of the period and low the remaining 80%. In most cases, averaging the on and the off times over a long period of time is translated into the relative power used by the load.

We are able to combine the current direction control circuit with the PWM signal through the use of an AND gate that mixes the two signals (figure 1.30 (a)). For simplicity, we drive the PWM-direction control combined signal only through the lower MOSFETs, while leaving the upper MOSFETs in a stable position. By controlling the duty cycle of this PWM signal, we

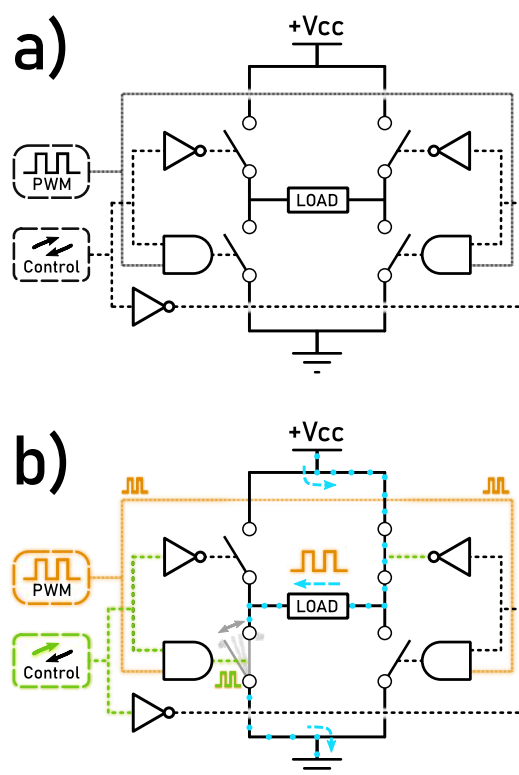


Figure 1.30: (a) H bridge conceptual schematics with current direction control circuit as well as PWM current control circuit. (b) Load current direction and PWM control operating simultaneously.

can control for how long the thermoelectric is on, modulating the effective heating or cooling power (figure 1.30 (b)). PWM operation, being a cyclical on/off operation mode, is not the most recommended for thermoelectric modules because of module degradation problems, as opposed to constant voltage operation. However, at high enough PWM frequencies, thermoelectric degradation is reported to be virtually equal.¹⁴²

This PWM signal is provided by an additional input, resulting in a circuit with only two digital inputs: one that controls the current direction, ultimately if we heat up or cool down the substrate; and another that controls the power we deliver in that mode, or how much we heat up or cool down the cell.

As a final touch, we added several protection components to the circuit to prevent current drops and to filter higher frequencies and voltage spikes caused by sudden load changes. We also added signaling capabilities so that the user can visually interact with the circuit and see when there is an overheating fault or if the modules are cooling down or heating up even when controlled by the Arduino. And for direct human interaction, we added buttons for the manual control and debugging of the system, allowing a user to manually heat up or cool down a sample if desired (figure 1.31).

The resulting circuit can be viewed in detail in figure 1.32, with all the sub-circuits separated in relation to their function. The schematics as well as the PCB layout are open source and can be found in the public repository located in the link below, or by scanning the QR code from figure 1.12:

https://github.com/minusmagis/Nanopto_Hot_n_Cold_PCB

1.C Drift Diffusion Simulations Supplementary



Figure 1.31: Manual circuit operation in cooling mode where the green LED indicates that the board receives power, and the blue LED indicates that it is currently cooling the sample.

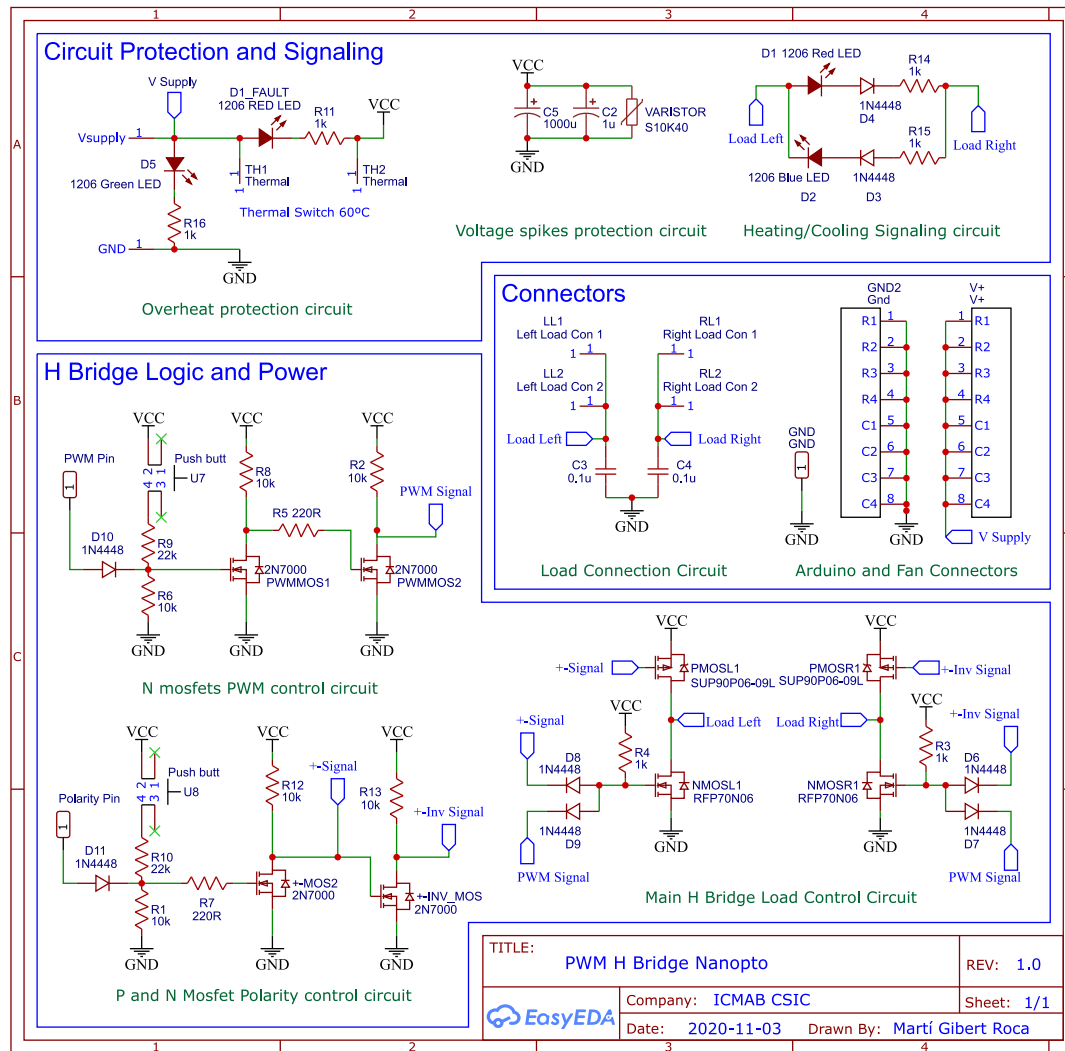


Figure 1.32: Schematics of the “Hot n’ cold” PWM H bridge temperature control circuit, showing the different sub-circuits and a brief explanation of their function.

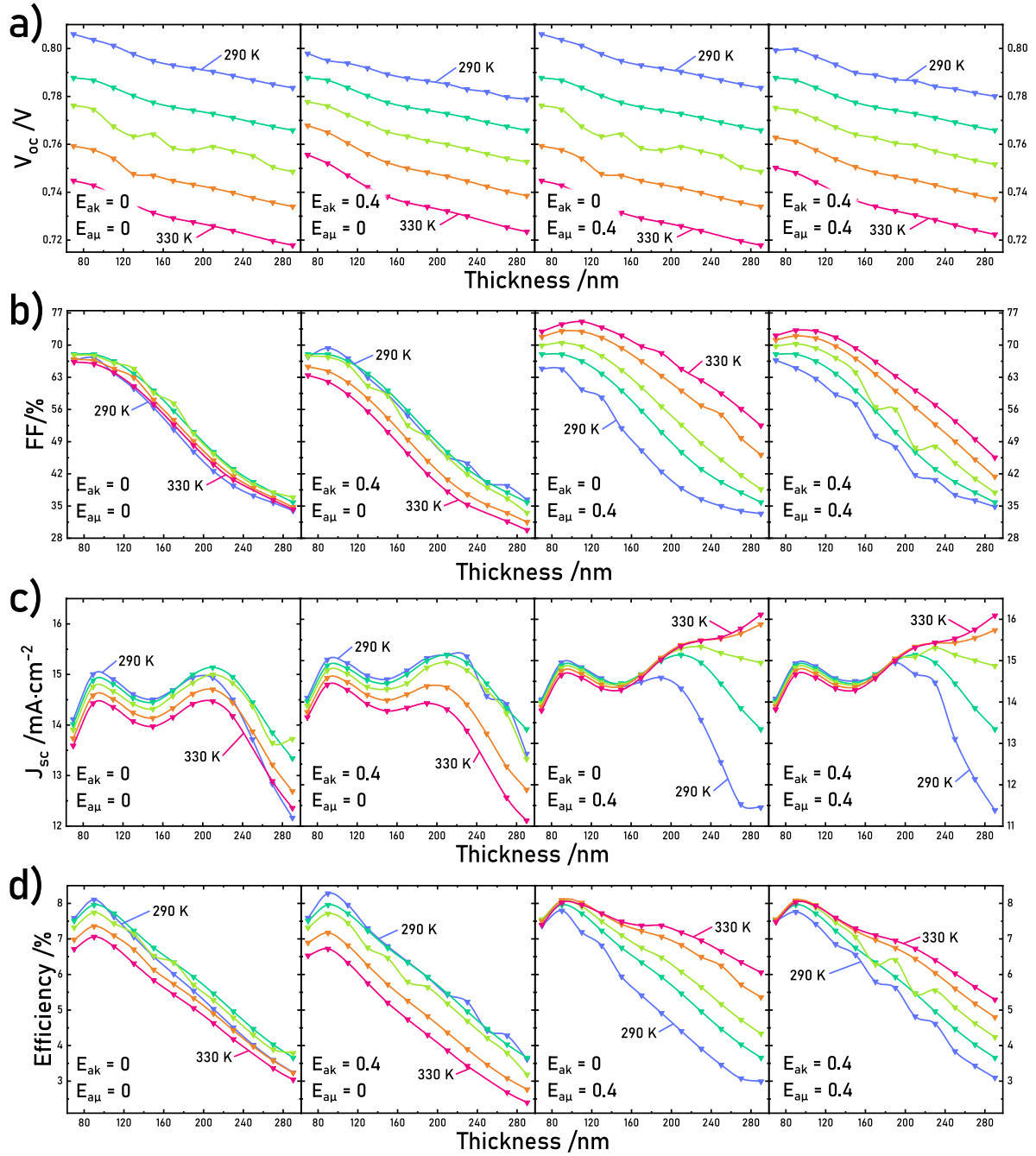


Figure 1.33: Comparison table for all drift diffusion simulation results explained in section 1.5.2, including from top to bottom: V_{oc} ; FF; J_{sc} ; and efficiency.

Bibliography

- ¹ José P. Jurado, Bernhard Döring, Osnat Zapata-Arteaga, Alejandro R. Goñi, and Mariano Campoy-Quiles. Comparing different geometries for photovoltaic-thermoelectric hybrid devices based on organics. *Journal of Materials Chemistry C*, 9(6):2123–2132, 2021.
- ² M Azzouzi, J Nelson, F Eisner, N Gallop, J Yan, X Zheng, H Cha, Q He, Z Fei, M Heeney, and A Bakulin. Reconciling models of interfacial state kinetics and device performance in organic solar cells: Impact of the energy offsets on the power conversion efficiency. *Energy and Environmental Science*, 2022.
- ³ E.A. Sjerps-Koomen, E.A. Alsema, and W.C. Turkenburg. A simple model for PV module reflection losses under field conditions. *Solar Energy*, 57(6):421–432, 12 1996.
- ⁴ Karen Forberich, Gilles Dennler, Markus C. Scharber, Kurt Hingerl, Thomas Fromherz, and Christoph J. Brabec. Performance improvement of organic solar cells with moth eye anti-reflection coating. *Thin Solid Films*, 516(20):7167–7170, 2008.
- ⁵ A. Scheydecker, A. Goetzberger, and V. Wittwer. Reduction of reflection losses of PV-modules by structured surfaces. *Solar Energy*, 53(2):171–176, 8 1994.
- ⁶ K. Rajkanan, R. Singh, and J. Shewchun. Absorption coefficient of silicon for solar cell calculations. *Solid-State Electronics*, 22(9):793–795, 9 1979.
- ⁷ Zhaosheng Hu, Zhenhua Lin, Jie Su, Jincheng Zhang, Jingjing Chang, and Yue Hao. A Review on Energy Band-Gap Engineering for Perovskite Photovoltaics. *Solar RRL*, 3(12):1–9, 2019.

- ⁸ Lingg, Buecheler, and Tiwari. Review of CdTe1–xSex Thin Films in Solar Cell Applications. *Coatings*, 9(8):520, 8 2019.
- ⁹ I. M. Dharmadasa. Third generation multi-layer tandem solar cells for achieving high conversion efficiencies. *Solar Energy Materials and Solar Cells*, 85(2):293–300, 2005.
- ¹⁰ M. W. Wanlass, J. S. Ward, K. A. Emery, T. A. Gessert, C. R. Osterwald, and T. J. Coutts. High-performance concentrator tandem solar cells based on IR-sensitive bottom cells. *Solar Cells*, 30(1-4):363–371, 1991.
- ¹¹ Bennett Widyolar, Lun Jiang, Mahmoud Abdelhamid, and Roland Winston. Design and modeling of a spectrum-splitting hybrid CSP-CPV parabolic trough using two-stage high concentration optics and dual junction InGaP/GaAs solar cells. *Solar Energy*, 165(August 2017):75–84, 2018.
- ¹² Zhengshan J. Yu, Kathryn C. Fisher, Brian M. Wheelwright, Roger P. Angel, and Zachary C. Holman. PVMirror: A New Concept for Tandem Solar Cells and Hybrid Solar Converters. *IEEE Journal of Photovoltaics*, 5(6):1791–1799, 2015.
- ¹³ Xinjing Huang, Dejiu Fan, and Stephen R. Forrest. Scalable semitransparent prototype organic photovoltaic module with minimal resistance loss. *Organic Electronics*, 97(May):106276, 2021.
- ¹⁴ Xin Xiao, Kyusang Lee, and Stephen R. Forrest. Scalability of multi-junction organic solar cells for large area organic solar modules. *Applied Physics Letters*, 106(21), 2015.
- ¹⁵ Xing Ju, Chao Xu, Yangqing Hu, Xue Han, Gaosheng Wei, and Xiaoze Du. A review on the development of photovoltaic/concentrated solar power (PV-CSP) hybrid systems. *Solar Energy Materials and Solar Cells*, 161(December 2016):305–327, 2017.
- ¹⁶ Priyanka Singh and N. M. Ravindra. Temperature dependence of solar cell performance - An analysis. *Solar Energy Materials and Solar Cells*, 101:36–45, 2012.

- ¹⁷ John C.C. Fan. Theoretical temperature dependence of solar cell parameters. *Solar Cells*, 17(2-3):309–315, 4 1986.
- ¹⁸ Priyanka Singh, S. N. Singh, M. Lal, and M. Husain. Temperature dependence of I-V characteristics and performance parameters of silicon solar cell. *Solar Energy Materials and Solar Cells*, 92(12):1611–1616, 2008.
- ¹⁹ Taesoo D. Lee and Abasifreke U. Ebong. A review of thin film solar cell technologies and challenges. *Renewable and Sustainable Energy Reviews*, 70(September 2015):1286–1297, 2017.
- ²⁰ A. B. Sproul, M. A. Green, and J. Zhao. Improved value for the silicon intrinsic carrier concentration at 300 K. *Applied Physics Letters*, 57(3):255–257, 1990.
- ²¹ Martin A. Green. General temperature dependence of solar cell performance and implications for device modelling. *Progress in Photovoltaics: Research and Applications*, 11(5):333–340, 2003.
- ²² Sewang Yoon and Vahan Garboushian. Reduced temperature dependence of high-concentration photovoltaic solar cell open-circuit voltage (Voc) at high concentration levels. *Conference Record of the IEEE Photovoltaic Specialists Conference*, 2(310):1500–1504, 1994.
- ²³ M. K. El-Adawi and I. A. Al-Nuaim. The temperature functional dependence of VOC for a solar cell in relation to its efficiency new approach. *Desalination*, 209(1-3 SPEC. ISS.):91–96, 2007.
- ²⁴ Quinn Burlingame, Gloria Zanotti, Laura Ciammaruchi, Eugene A. Katz, and Stephen R. Forrest. Outdoor operation of small-molecule organic photovoltaics. *Organic Electronics*, 41:274–279, 2017.
- ²⁵ J. G. Kushmerick, S. K. Pollack, J. C. Yang, J. Naciri, D. B. Holt, M. A. Ratner, and R. Shashidhar. Understanding Charge Transport in Molecular Electronics. *Annals of the New York Academy of Sciences*, 1006:277–290, 2003.

- ²⁶ Hemant Kumar, Pankaj Kumar, Neeraj Chaudhary, Ramil Bhardwaj, Suresh Chand, S. C. Jain, and Vikram Kumar. Effect of temperature on the performance of CuPc/C60 photovoltaic device. *Journal of Physics D: Applied Physics*, 42(1), 2009.
- ²⁷ D. Chirvase, J. Parisi, J. C. Hummelen, and V. Dyakonov. Influence of nanomorphology on the photovoltaic action of polymer-fullerene composites. *Nanotechnology*, 15(9):1317–1323, 2004.
- ²⁸ W. Bagienski and M. C. Gupta. Temperature dependence of polymer/fullerene organic solar cells. *Solar Energy Materials and Solar Cells*, 95(3):933–941, 2011.
- ²⁹ Lichang Zeng, Ching W. Tang, and Shaw H. Chen. Effects of active layer thickness and thermal annealing on polythiophene: Fullerene bulk heterojunction photovoltaic devices. *Applied Physics Letters*, 97(5):1–4, 2010.
- ³⁰ M. S. Ulum, E. Sesa, Kasman, and W. Belcher. The effect of active layer thickness on P3HT:PCBM nanoparticulate organic photovoltaic device performance. *Journal of Physics: Conference Series*, 1242(1), 2019.
- ³¹ Sebastian Pont, James R. Durrant, and João T. Cabral. Dynamic PCBM:Dimer Population in Solar Cells under Light and Temperature Fluctuations. *Advanced Energy Materials*, 9(19):1–9, 2019.
- ³² Infinity PV Source/Sink measure unit (SMU), 2022.
- ³³ LITOS — FLUXIM — Stability tests on organic and perovskite solar cells and LEDs, 2022.
- ³⁴ Solar Cell I-V Test System — Ossila, 2022.
- ³⁵ Hiroyuki Saeki, Omi Kurimoto, Haruka Nakaoka, Masahiro Misaki, Daiki Kuzuhara, Hiroko Yamada, Kenji Ishida, and Yasukiyo Ueda. Effect of crystallinity in small molecular weight organic heterojunction solar cells. *Journal of Materials Chemistry C*, 2(27):5357–5364, 2014.

- ³⁶ Biswajit Ray and Muhammad A. Alam. A compact physical model for morphology induced intrinsic degradation of organic bulk heterojunction solar cell. *Applied Physics Letters*, 99(3):1–4, 2011.
- ³⁷ Biswajit Ray, Pradeep R. Nair, and Muhammad A. Alam. Annealing dependent performance of organic bulk-heterojunction solar cells: A theoretical perspective. *Solar Energy Materials and Solar Cells*, 95(12):3287–3294, 2011.
- ³⁸ Sung Kyu Park, Yong Hoon Kim, and Jeong In Han. Effect of annealing treatment and surface morphology on power conversion in organic photovoltaics. *Japanese Journal of Applied Physics*, 48(8 Part 1):0815051–0815053, 2009.
- ³⁹ Maher Al-Ibrahim, Oliver Ambacher, Steffi Sensfuss, and Gerhard Gobsch. Effects of solvent and annealing on the improved performance of solar cells based on poly(3-hexylthiophene): Fullerene. *Applied Physics Letters*, 86(20):1–3, 2005.
- ⁴⁰ Zuo Yi, Wang Ni, Qian Zhang, Miaomiao Li, Bin Kan, Xiangjian Wan, and Yongsheng Chen. Effect of thermal annealing on active layer morphology and performance for small molecule bulk heterojunction organic solar cells. *Journal of Materials Chemistry C*, 2(35):7247–7255, 2014.
- ⁴¹ S Pingel, D Koshnicharov, O Frank, and T Geipel. Initial degradation of industrial silicon solar cells in solar panels’. *25th EU PVSEC*, (January), 2010.
- ⁴² D. Zhang, A. Tavakoliyaraki, Y. Wu, R. A.C.M.M. Van Swaaij, and M. Zeman. Influence of ITO deposition and post annealing on HIT solar cell structures. *Energy Procedia*, 8(April):207–213, 2011.
- ⁴³ Suren A. Gevorgyan, Mikkel Jørgensen, and Frederik C. Krebs. A setup for studying stability and degradation of polymer solar cells. *Solar Energy Materials and Solar Cells*, 92(7):736–745, 2008.

- ⁴⁴ Shunsuke Kijima and Tokio Nakada. High-temperature degradation mechanism of Cu(In,Ga)Se₂-based thin film solar cells. *Applied Physics Express*, 1(7):0750021–0750023, 2008.
- ⁴⁵ Juan Bisquert and Emilio J. Juarez-Perez. The Causes of Degradation of Perovskite Solar Cells. *Journal of Physical Chemistry Letters*, 10(19):5889–5891, 2019.
- ⁴⁶ Lilian Chang, Hans W.A. Lademann, Jörg Bernd Bonekamp, Klaus Meerholz, and Adam J. Moulé. Effect of trace solvent on the morphology of P3HT:PCBM bulk heterojunction solar cells. *Advanced Functional Materials*, 21(10):1779–1787, 2011.
- ⁴⁷ Barry C. Thompson and Jean M.J. Fréchet. Polymer-fullerene composite solar cells. *Angewandte Chemie - International Edition*, 47(1):58–77, 2008.
- ⁴⁸ Nikhil Chander, Sujata Singh, and S. Sundar Kumar Iyer. Stability and reliability of P3HT:PC61BM inverted organic solar cells. *Solar Energy Materials and Solar Cells*, 161(December 2016):407–415, 2017.
- ⁴⁹ Antonio Agresti, Sara Pescetelli, Yan Busby, and Tom Aernouts. Thermally Induced Fullerene Domain Coarsening Process in Organic Solar Cells. *IEEE Transactions on Electron Devices*, 66(1):678–688, 2019.
- ⁵⁰ Letian Dou, Chun Chao Chen, Ken Yoshimura, Kenichiro Ohya, Wei Hsuan Chang, Jing Gao, Yongsheng Liu, Eric Richard, and Yang Yang. Synthesis of 5H-dithieno[3,2-b:2',3'-d]pyran as an electron-rich building block for donor-acceptor type low-bandgap polymers. *Macromolecules*, 46(9):3384–3390, 2013.
- ⁵¹ Xiaowei Zhan, Zhan'ao Tan, Benoit Domercq, Zesheng An, Xuan Zhang, Stephen Barlow, Yongfang Li, Daoben Zhu, Bernard Kippelen, and Seth R. Marder. A high-mobility electron-transport polymer with broad absorption and its use in field-effect transistors and all-polymer solar cells. *Journal of the American Chemical Society*, 129(23):7246–7247, 2007.

- ⁵² Pei Cheng, Qinqin Shi, Yuze Lin, Yongfang Li, and Xiaowei Zhan. Evolved structure of thiazolothiazole based small molecules towards enhanced efficiency in organic solar cells. *Organic Electronics*, 14(2):599–606, 2013.
- ⁵³ Isabel Fraga Domínguez, Andreas Distler, and Larry Lüer. Stability of Organic Solar Cells: The Influence of Nanostructured Carbon Materials. *Advanced Energy Materials*, 7(10), 2017.
- ⁵⁴ Sabine Bertho, Griet Janssen, Thomas J. Cleij, Bert Conings, Wouter Moons, Abay Gadisa, Jan D’Haen, Etienne Goovaerts, Laurence Lutsen, Jean Manca, and Dirk Vanderzande. Effect of temperature on the morphological and photovoltaic stability of bulk heterojunction polymer:fullerene solar cells. *Solar Energy Materials and Solar Cells*, 92(7):753–760, 2008.
- ⁵⁵ N. Bristow and J. Kettle. Outdoor organic photovoltaic module characteristics: Benchmarking against other PV technologies for performance, calculation of Ross coefficient and outdoor stability monitoring. *Solar Energy Materials and Solar Cells*, 175(July 2017):52–59, 2018.
- ⁵⁶ Minwoo Nam, Jaehong Yoo, Yunjae Park, Hye Yeon Noh, Yongkook Park, Junhee Cho, Jung A. Kim, Jehan Kim, Hyun Hwi Lee, Rakwoo Chang, and Doo Hyun Ko. Ternary blend organic solar cells with improved morphological stability. *Journal of Materials Chemistry A*, 7(16):9698–9707, 2019.
- ⁵⁷ Thanh Luan Nguyen, Tack Ho Lee, Bhoj Gautam, Song Yi Park, Kenan Gundogdu, Jin Young Kim, and Han Young Woo. Single Component Organic Solar Cells Based on Oligothiophene-Fullerene Conjugate. *Advanced Functional Materials*, 27(39):1–9, 2017.
- ⁵⁸ Christoph J. Schaffer, Claudia M. Palumbiny, Martin A. Niedermeier, Christian Jendrzewski, Gonzalo Santoro, Stephan V. Roth, and Peter Müller-Buschbaum. A direct evidence of morphological degradation on a nanometer scale in polymer solar cells. *Advanced Materials*, 25(46):6760–6764, 2013.
- ⁵⁹ Gary A. Brehm and Victor A. Bloomfield. Analysis of Polydispersity in Polymer Solutions by Inelastic Laser Light Scattering. *Macromolecules*, 8(5):663–665, 1975.

- ⁶⁰ P. G. de Gennes. *Scaling Concepts in Polymer Physics*. Cornell University Press, Ithaca and London, 6 1979.
- ⁶¹ Tao Wang, Andrew J. Pearson, Alan D.F. Dunbar, Paul A. Staniec, Darren C. Watters, Hunan Yi, Anthony J. Ryan, Richard A.L. Jones, Ahmed Iraqi, and David G. Lidzey. Correlating structure with function in thermally annealed PCDTBT:PC 70BM photovoltaic blends. *Advanced Functional Materials*, 22(7):1399–1408, 2012.
- ⁶² Huanqi Cao, Weidong He, Yiwu Mao, Xiao Lin, Ken Ishikawa, James H. Dickerson, and Wayne P. Hess. Recent progress in degradation and stabilization of organic solar cells. *Journal of Power Sources*, 264:168–183, 2014.
- ⁶³ Andrea Gasperini, Xavier A. Jeanbourquin, Aiman Rahmanudin, Xiaoyun Yu, and Kevin Sivula. Enhancing the Thermal Stability of Solution-Processed Small-Molecule Semiconductor Thin Films Using a Flexible Linker Approach. *Advanced Materials*, 27(37):5541–5546, 2015.
- ⁶⁴ Gianmarco Griffini, Jessica D. Douglas, Claudia Piliago, Thomas W. Holcombe, Stefano Turri, Jean M.J. Fréchet, and Justin L. Mynar. Long-term thermal stability of high-efficiency polymer solar cells based on photocrosslinkable donor-acceptor conjugated polymers. *Advanced Materials*, 23(14):1660–1664, 2011.
- ⁶⁵ Leiping Duan, Haimang Yi, Yu Zhang, Faiazul Haque, Cheng Xu, and Ashraf Uddin. Comparative study of light- and thermal-induced degradation for both fullerene and non-fullerene-based organic solar cells. *Sustainable Energy and Fuels*, 3(3):723–735, 2019.
- ⁶⁶ I. T. Sachs-Quintana, Thomas Heumüller, William R. Mateker, Darian E. Orozco, Rongrong Checharoen, Sean Sweetnam, Christoph J. Brabec, and Michael D. McGehee. Electron barrier formation at the organic-back contact interface is the first step in thermal degradation of polymer solar cells. *Advanced Functional Materials*, 24(25):3978–3985, 2014.
- ⁶⁷ Erich Wimmer, Walter Wolf, Jürgen Sticht, Paul Saxe, Clint B. Geller, Reza Najafabadi, and George A. Young. Temperature-dependent diffusion coefficients from ab initio computations:

- Hydrogen, deuterium, and tritium in nickel. *Physical Review B - Condensed Matter and Materials Physics*, 77(13):1–12, 2008.
- ⁶⁸ J. D. McBrayer, R. M. Swanson, and T. W. Sigmon. Diffusion of Metals in Silicon Dioxide. *Journal of The Electrochemical Society*, 133(6):1242–1246, 1986.
- ⁶⁹ Kai Zhang, Ruoxi Xia, Baobing Fan, Xiang Liu, Zhenfeng Wang, Sheng Dong, Hin Lap Yip, Lei Ying, Fei Huang, and Yong Cao. 11.2% All-Polymer Tandem Solar Cells with Simultaneously Improved Efficiency and Stability. *Advanced Materials*, 30(36):1–8, 2018.
- ⁷⁰ W. Greenbank, N. Rolston, E. Destouesse, G. Wantz, L. Hirsch, R. Dauskardt, and S. Cham-bon. Improved mechanical adhesion and electronic stability of organic solar cells with thermal ageing: the role of diffusion at the hole extraction interface. *Journal of Materials Chemistry A*, 5(6):2911–2919, 2017.
- ⁷¹ Yawen Li, Tengfei Li, and Yuze Lin. Stability: Next focus in organic solar cells based on non-fullerene acceptors. *Materials Chemistry Frontiers*, 5(7):2907–2930, 2021.
- ⁷² Wei Li, Mengxue Chen, Jinlong Cai, Emma L.K. Spooner, Huijun Zhang, Robert S. Gurney, Dan Liu, Zuo Xiao, David G. Lidzey, Liming Ding, and Tao Wang. Molecular Order Control of Non-fullerene Acceptors for High-Efficiency Polymer Solar Cells. *Joule*, 3(3):819–833, 2019.
- ⁷³ Wenchao Zhao, Deping Qian, Shaoqing Zhang, Sunsun Li, Olle Inganäs, Feng Gao, and Jianhui Hou. Fullerene-Free Polymer Solar Cells with over 11% Efficiency and Excellent Thermal Stability. *Advanced Materials*, 28(23):4734–4739, 2016.
- ⁷⁴ Wei Li, Zuo Xiao, Jinlong Cai, Joel A. Smith, Emma L.K. Spooner, Rachel C. Kilbride, Onkar S. Game, Xianyi Meng, Donghui Li, Huijun Zhang, Mengxue Chen, Robert S. Gurney, Dan Liu, Richard A.L. Jones, David G. Lidzey, Liming Ding, and Tao Wang. Correlating the electron-donating core structure with morphology and performance of carbon–oxygen-bridged ladder-type non-fullerene acceptor based organic solar cells. *Nano Energy*, 61(April):318–326, 2019.

- ⁷⁵ Masoud Ghasemi, Huawei Hu, Zhengxing Peng, Jeromy James Rech, Indunil Angunawela, Joshua H. Carpenter, Samuel J. Stuard, Andrew Wadsworth, Iain McCulloch, Wei You, and Harald Ade. Delineation of Thermodynamic and Kinetic Factors that Control Stability in Non-fullerene Organic Solar Cells. *Joule*, 3(5):1328–1348, 2019.
- ⁷⁶ Davide Bartesaghi, Irene Del Carmen Pérez, Juliane Kniepert, Steffen Roland, Mathieu Turbiez, Dieter Neher, and L. Jan Anton Koster. Competition between recombination and extraction of free charges determines the fill factor of organic solar cells. *Nature Communications*, 6(May):2–11, 2015.
- ⁷⁷ Christopher M. Proctor, Chunki Kim, Dieter Neher, and Thuc Quyen Nguyen. Nongeminate recombination and charge transport limitations in diketopyrrolopyrrole-based solution-processed small molecule solar cells. *Advanced Functional Materials*, 23(28):3584–3594, 2013.
- ⁷⁸ Thomas Kirchartz, Tiziano Agostinelli, Mariano Campoy-Quiles, Wei Gong, and Jenny Nelson. Understanding the thickness-dependent performance of organic bulk heterojunction solar cells: The influence of mobility, lifetime, and space charge. *Journal of Physical Chemistry Letters*, 3(23):3470–3475, 2012.
- ⁷⁹ Ralf Mauer, Ian A. Howard, and Frédéric Laquai. Effect of nongeminate recombination on fill factor in polythiophene/ methanofullerene organic solar cells. *Journal of Physical Chemistry Letters*, 1(24):3500–3505, 2010.
- ⁸⁰ Lili Wu, Huidong Zang, Yu Che Hsiao, Xitian Zhang, and Bin Hu. Origin of the fill factor loss in bulk-heterojunction organic solar cells. *Applied Physics Letters*, 104(15), 2014.
- ⁸¹ D. Chirvase, Z. Chiguvare, M. Knipper, J. Parisi, V. Dyakonov, and J. C. Hummelen. Temperature dependent characteristics of poly(3 hexylthiophene)-fullerene based heterojunction organic solar cells. *Journal of Applied Physics*, 93(6):3376–3383, 2003.
- ⁸² V.D. Mihailetschi, J.K.J. van Duren, P.W.M. Blom, J.C. Hummelen, R.A.J. Janssen, J.M. Kroon, M.T. Rispens, W.J.H. Verhees, and M.M. Wienk. Electron Transport in a Methanofullerene. *Advanced Functional Materials*, 13(1):43–46, 1 2003.

- ⁸³ Donggu Lee, Junmo Kim, Gyeongtae Park, Hyeong Woo Bae, Myungchan An, and Jun Young Kim. Enhanced operating temperature stability of organic solar cells with metal oxide hole extraction layer. *Polymers*, 12(4):1–9, 2020.
- ⁸⁴ Yannan Zhang, Yalong Xu, Michael J. Ford, Fangchao Li, Jianxia Sun, Xufeng Ling, Yongjie Wang, Jinan Gu, Jianyu Yuan, and Wanli Ma. Thermally Stable All-Polymer Solar Cells with High Tolerance on Blend Ratios. *Advanced Energy Materials*, 8(18):1–10, 2018.
- ⁸⁵ Christopher J.M. Emmott, Davide Moia, Philip Sandwell, Nicholas Ekins-Daukes, Markus Hösel, Lukas Lukoschek, Charith Amarasinghe, Frederik C. Krebs, and Jenny Nelson. In-situ, long-term operational stability of organic photovoltaics for off-grid applications in Africa. *Solar Energy Materials and Solar Cells*, 149:284–293, 2016.
- ⁸⁶ Giorgio Bardizza, Elena Salis, Carlos Toledo, and Ewan D. Dunlop. Power performance and thermal operation of organic photovoltaic modules in real operating conditions. *Progress in Photovoltaics: Research and Applications*, 28(6):593–600, 2020.
- ⁸⁷ Yiwei Zhang, Ifor D.W. Samuel, Tao Wang, and David G. Lidzey. Current Status of Outdoor Lifetime Testing of Organic Photovoltaics, 8 2018.
- ⁸⁸ Siddhartha Chhabra and Yan Solihin. Green secure processors: Towards power-efficient secure processor design. *Lecture Notes in Computer Science (including subseries Lecture Notes in Artificial Intelligence and Lecture Notes in Bioinformatics)*, 6340(PART 1):329–351, 2010.
- ⁸⁹ Yun Zhang, Huifeng Yao, Shaoqing Zhang, Yunpeng Qin, Jianqi Zhang, Liyan Yang, Wanning Li, Zhixiang Wei, Feng Gao, and Jianhui Hou. Fluorination vs. chlorination: a case study on high performance organic photovoltaic materials. *Science China Chemistry*, 61(10):1328–1337, 2018.
- ⁹⁰ Eric Verploegen, Rajib Mondal, Christopher J. Bettinger, Seihout Sok, Michael F. Toney, and Zhenan Bao. Effects of thermal annealing upon the morphology of polymer-fullerene blends. *Advanced Functional Materials*, 20(20):3519–3529, 2010.

- ⁹¹ Zhen Wang, Yaowen Nian, Haiying Jiang, Feilong Pan, Zelong Hu, Lianjie Zhang, Yong Cao, and Junwu Chen. High Voc ternary nonfullerene polymer solar cells with improved efficiency and good thermal stability. *Organic Electronics*, 69(March):174–180, 2019.
- ⁹² Qiuju Liang, Xuechen Jiao, Ye Yan, Zhiyuan Xie, Guanghao Lu, Jiangang Liu, and Yanchun Han. Separating Crystallization Process of P3HT and O-IDTBR to Construct Highly Crystalline Interpenetrating Network with Optimized Vertical Phase Separation. *Advanced Functional Materials*, 29(47):1–12, 2019.
- ⁹³ Mariano Campoy-Quiles, M. Isabel Alonso, Donal D.C. Bradley, and Lee J. Richter. Advanced ellipsometric characterization of conjugated polymer films. *Advanced Functional Materials*, 24(15):2116–2134, 2014.
- ⁹⁴ Germ Garcia-Belmonte. Temperature dependence of open-circuit voltage in organic solar cells from generation-recombination kinetic balance. *Solar Energy Materials and Solar Cells*, 94(12):2166–2169, 2010.
- ⁹⁵ S. D. Baranovskii. Theoretical description of charge transport in disordered organic semiconductors. *Physica Status Solidi (B) Basic Research*, 251(3):487–525, 2014.
- ⁹⁶ Mushfika Baishakhi Upama, Matthew Wright, Md Arafat Mahmud, Naveen Kumar Elumalai, Arman Mahboubi Soufiani, Dian Wang, Cheng Xu, and Ashraf Uddin. Photodegradation of high efficiency fullerene-free polymer solar cells. *Nanoscale*, 9(47):18788–18797, 2017.
- ⁹⁷ Sara Marina, Edgar Gutierrez-Fernandez, Junkal Gutierrez, Marco Gobbi, Nicolás Ramos, Eduardo Solano, Jeromy Rech, Wei You, Luis Hueso, Agnieszka Tercjak, Harald Ade, and Jaime Martin. Semi-paracrystallinity in semi-conducting polymers. *Materials Horizons*, 2022.
- ⁹⁸ Liyang Yu, Deping Qian, Sara Marina, Ferry A.A. Nugroho, Anirudh Sharma, Sandra Hultmark, Anna I. Hofmann, Renee Kroon, Johannes Benduhn, Detlef M. Smilgies, Koen Vandewal, Mats R. Andersson, Christoph Langhammer, Jaime Martín, Feng Gao, and Christian

- Müller. Diffusion-Limited Crystallization: A Rationale for the Thermal Stability of Non-Fullerene Solar Cells. *ACS Applied Materials and Interfaces*, 2019.
- ⁹⁹ Laura Ciammaruchi, Osnat Zapata-Arteaga, Edgar Gutiérrez-Fernández, Jaime Martin, and Mariano Campoy-Quiles. Structure dependent photostability of ITIC and ITIC-4F. *Materials Advances*, 1(8):2846–2861, 2020.
- ¹⁰⁰ Thomas J. Aldrich, Micaela Matta, Weigang Zhu, Steven M. Swick, Charlotte L. Stern, George C. Schatz, Antonio Facchetti, Ferdinand S. Melkonyan, and Tobin J. Marks. Fluorination Effects on Indacenodithienothiophene Acceptor Packing and Electronic Structure, End-Group Redistribution, and Solar Cell Photovoltaic Response. *Journal of the American Chemical Society*, 141:3274–3287, 2019.
- ¹⁰¹ Qiuju Liang, Jie Han, Chunpeng Song, Xinhong Yu, Detlef M. Smilgies, Kui Zhao, Jiangang Liu, and Yanchun Han. Reducing the confinement of PBDB-T to ITIC to improve the crystallinity of PBDB-T/ITIC blends. *Journal of Materials Chemistry A*, 6(32):15610–15620, 2018.
- ¹⁰² I. I. Fishchuk, A. K. Kadashchuk, J. Genoe, Mujeeb Ullah, H. Sitter, Th B. Singh, N. S. Sariciftci, and H. Bässler. Temperature dependence of the charge carrier mobility in disordered organic semiconductors at large carrier concentrations. *Physical Review B - Condensed Matter and Materials Physics*, 81(4):1–12, 2010.
- ¹⁰³ Zhuping Fei, Flurin D. Eisner, Xuechen Jiao, Mohammed Azzouzi, Jason A. Röhr, Yang Han, Munazza Shahid, Anthony S.R. Chesman, Christopher D. Easton, Christopher R. McNeill, Thomas D. Anthopoulos, Jenny Nelson, and Martin Heeney. An Alkylated Indacenodithieno[3,2-b]thiophene-Based Nonfullerene Acceptor with High Crystallinity Exhibiting Single Junction Solar Cell Efficiencies Greater than 13% with Low Voltage Losses. *Advanced Materials*, 30(8), 2018.
- ¹⁰⁴ Mohammed Azzouzi. *Voltage Losses and Recombination Mechanisms in Organic Solar Cells*. PhD thesis, London Imperial College, 2020.

- ¹⁰⁵ Vincent M. Le Corre, Azadeh Rahimi Chatri, Nutifafa Y. Doumon, and L. Jan Anton Koster. Charge Carrier Extraction in Organic Solar Cells Governed by Steady-State Mobilities. *Advanced Energy Materials*, 7(22):1–7, 2017.
- ¹⁰⁶ N. J. Van Der Kaap and L. J.A. Koster. Charge carrier thermalization in organic diodes. *Scientific Reports*, 6:1–9, 2016.
- ¹⁰⁷ Palas Roy. Hot-carriers in organic photovoltaics. *Pure and Applied Chemistry*, 93(2):223–230, 2021.
- ¹⁰⁸ Artem A. Bakulin, Akshay Rao, Vlad G. Pavelyev, Paul H.M. Van Loosdrecht, Maxim S. Pshenichnikov, Dorota Niedzialek, Jérôme Cornil, David Beljonne, and Richard H. Friend. The role of driving energy and delocalized states for charge separation in organic semiconductors. *Science*, 335(6074):1340–1344, 2012.
- ¹⁰⁹ Pabitra K. Nayak, K. L. Narasimhan, and David Cahen. Separating charges at organic interfaces: Effects of disorder, hot states, and electric field. *Journal of Physical Chemistry Letters*, 4(10):1707–1717, 2013.
- ¹¹⁰ Jia Yue Yang and Ming Hu. Temperature-Induced Large Broadening and Blue Shift in the Electronic Band Structure and Optical Absorption of Methylammonium Lead Iodide Perovskite. *Journal of Physical Chemistry Letters*, 8(16):3720–3725, 2017.
- ¹¹¹ Derek Zomerman, Jessica Kong, Seth M. McAfee, Gregory C. Welch, and Timothy L. Kelly. Control and Characterization of Organic Solar Cell Morphology Through Variable-Pressure Solvent Vapor Annealing. *ACS Applied Energy Materials*, 1(10):5663–5674, 2018.
- ¹¹² L Vina. 8 of of. 1984.
- ¹¹³ K P O Donnell, X Chen, and X Chen. Temperature dependence of semiconductor band gaps dependence of semiconductor band gaps. 2924:67–70, 1991.
- ¹¹⁴ P. Lautenschlager, M. Garriga, S. Logothetidis, and M. Cardona. Interband critical points of GaAs and their temperature dependence. *Physical Review B*, 35(17):9174–9189, 6 1987.

- ¹¹⁵ KUN HUANG and AVRIL RHYS. Theory of light absorption and non-radiative transitions in F-centres. volume 204, pages 74–92. 4 2000.
- ¹¹⁶ Nikolaos Felekidis, Armantas Melianas, and Martijn Kemerink. Automated open-source software for charge transport analysis in single-carrier organic semiconductor diodes. *Organic Electronics*, 61(May):318–328, 2018.
- ¹¹⁷ Hwajeong Kim, Sungho Nam, Jaehoon Jeong, Sooyong Lee, Jooyeok Seo, Hyemi Han, and Youngkyoo Kim. Organic solar cells based on conjugated polymers: History and recent advances. *Korean Journal of Chemical Engineering*, 31(7):1095–1104, 2014.
- ¹¹⁸ Frederik C. Krebs, Thomas Tromholt, and Mikkell Jørgensen. Upscaling of polymer solar cell fabrication using full roll-to-roll processing. *Nanoscale*, 2(6):873–886, 2010.
- ¹¹⁹ Juan Bisquert, David Cahen, Gary Hodes, Sven Rühle, and Arie Zaban. Physical chemical principles of photovoltaic conversion with nanoparticulate, mesoporous dye-sensitized solar cells. *Journal of Physical Chemistry B*, 108(24):8106–8118, 2004.
- ¹²⁰ H. Bässler. Charge Transport in Disordered Organic Photoconductors a Monte Carlo Simulation Study. *Physica Status Solidi (B)*, 175(1):15–56, 1993.
- ¹²¹ A. V. Nenashev, J. O. Oelerich, and S. D. Baranovskii. Theoretical tools for the description of charge transport in disordered organic semiconductors. *Journal of Physics Condensed Matter*, 27(9), 2015.
- ¹²² Boyuan Qi and Jizheng Wang. Open-circuit voltage in organic solar cells. *Journal of Materials Chemistry*, 22(46):24315–24325, 2012.
- ¹²³ Barry P. Rand, Diana P. Burk, and Stephen R. Forrest. Offset energies at organic semiconductor heterojunctions and their influence on the open-circuit voltage of thin-film solar cells. *Physical Review B - Condensed Matter and Materials Physics*, 75(11):1–11, 2007.

- ¹²⁴ Wilfredo Nieves, Michael Ortiz-mojer, Juan C Orengo, and Clara Isaza. Enhancing the capability- to-affordability ratio of a manufacturing process : The didactic case of a 3D printer. (October), 2018.
- ¹²⁵ Robert A. Riggelman, Kenneth S. Schweizer, and Juan J. De Pablo. Nonlinear creep in a polymer glass. *Macromolecules*, 41(13):4969–4977, 2008.
- ¹²⁶ J. Raghavan and M. Meshii. Creep of Polymer Composites. *Composites Science and Technology*, 57(12):1673–1688, 1998.
- ¹²⁷ Seong Je Park, Ji Eun Lee, Jiyong Park, Nak Kyu Lee, Yong Son, and Suk Hee Park. High-temperature 3D printing of polyetheretherketone products: Perspective on industrial manufacturing applications of super engineering plastics. *Materials and Design*, 211:110163, 2021.
- ¹²⁸ Sun Xiaoyong, Cao Liangcheng, Ma Honglin, Gao Peng, Bai Zhanwei, and Li Cheng. Experimental analysis of high temperature PEEK materials on 3D printing test. *Proceedings - 9th International Conference on Measuring Technology and Mechatronics Automation, ICMTMA 2017*, pages 13–16, 2017.
- ¹²⁹ Zhichao Liu, Gong Wang, Yu Huo, and Wei Zhao. Research on precise control of 3D print nozzle temperature in PEEK material. *AIP Conference Proceedings*, 1890(October 2017), 2017.
- ¹³⁰ Elahesh Sirjani, Peter J. Cragg, and Marcus K. Dymond. Glass transition temperatures, melting temperatures, water contact angles and dimensional precision of simple fused deposition model 3D prints and 3D printed channels constructed from a range of commercially available filaments. *Chemical Data Collections*, 22:100244, 2019.
- ¹³¹ Miftahur Rahman, N. R. Schott, and Lakshmi Kanta Sadhu. Glass Transition of ABS in 3D Printing. *Comsol Boston 2016*, page 3, 2016.

- ¹³² Natalia von Windheim, David W Collinson, Trent Lau, L Catherine Brinson, and Ken Gall. The influence of porosity, crystallinity and interlayer adhesion on the tensile strength of 3D printed polylactic acid (PLA). *Rapid Prototyping Journal*, 27(7):1327–1336, 1 2021.
- ¹³³ Yuhan Liao, Chang Liu, Bartolomeo Coppola, Giuseppina Barra, Luciano Di Maio, Loredana Incarnato, and Khalid Lafdi. Effect of Porosity and Crystallinity on 3D Printed PLA Properties. *Polymers*, 11(9):1487, 9 2019.
- ¹³⁴ Ondrej Stava, Juraj Vanek, Bedrich Benes, Nathan Carr, and Radomír Měch. Stress relief: Improving structural strength of 3D printable objects. *ACM Transactions on Graphics*, 31(4):1–11, 2012.
- ¹³⁵ Sun Kon Lee, Yong Rae Kim, Su Hyun Kim, and Joo Hyung Kim. Investigation of the Internal Stress Relaxation in FDM 3D Printing : Annealing Conditions. *The Korean Society of Manufacturing Process Engineers*, 17(4):130–136, 2018.
- ¹³⁶ Hong-Cheol Kim, Da-Yeong Kim, Ji-Eun Lee, and Keun Park. Improvement of mechanical properties and surface finish of 3d-printed polylactic acid parts by constrained remelting. *Advanced Materials Letters*, 8(12):1199–1203, 2017.
- ¹³⁷ Steve Hermann. Testing the strength of 3D prints re-melted in salt — CNC Kitchen.
- ¹³⁸ Agnieszka Szust and Grzegorz Adamski. Using thermal annealing and salt remelting to increase tensile properties of 3D FDM prints. *Engineering Failure Analysis*, 132(November 2021):105932, 2022.
- ¹³⁹ S. Singh, A. Rajeshkannan, S. Feroz, and A. K. Jeevanantham. Effect of Normalizing on the Tensile Strength, Shrinkage and Surface Roughness of PLA Plastic. *Materials Today: Proceedings*, 24:1174–1182, 2020.
- ¹⁴⁰ SHIZUWO SANO. Theory of Thermoelectricity. *Tokyo Sugaku-Buturigakkwai Kizi Dai 2 Ki*, 4(1):2–26, 1907.

- ¹⁴¹ J. Parker. XXXVIII. On thermoelectric phenomena. *The London, Edinburgh, and Dublin Philosophical Magazine and Journal of Science*, 26(161):353–360, 10 1888.
- ¹⁴² Olivier Mellin and Florent Muret. Driving a Peltier Element (TEC): Efficiency and Aging. (July 2019):1–7, 2019.